Title	効率的で低コストな有機太陽電池のための作製プロセスの開発
Author(s)	Razali, Nur Tahirah Binti
Citation	
Issue Date	2014-12
Type	Thesis or Dissertation
Text version	ETD
URL	http://hdl.handle.net/10119/12620
Rights	
Description	Supervisor:村田　英幸, マテリアルサイエンス研究科, 博士

Development of Fabrication Processes for Efficient and Low Cost Organic Solar Cells

Nur Tahirah Razali

Japan Advanced Institute of Science and Technology

Doctoral Dissertation

Development of Fabrication Processes for Efficient and Low Cost Organic Solar Cells

Nur Tahirah Razali

Supervisor: Professor Dr. Hideyuki Murata
School of Materials Science
Japan Advanced Institute of Science and Technology

December 2014

Abstract

The development of fabrication processes in terms of morphological changes and vacuum free process for efficient and low cost organic solar cells (OSC) has been studied. The effect of annealing and interlayer to the device performances were investigated. Devices that were post-annealing after top electrode deposition have increased the solar cell performances significantly as compared to that of the devices without post-annealing. Post-annealing induced polymer crystallization and resulting in enhancement in the absorption. Vertical phase segregation also could occur as a result of annealing. In regular bulk heterojunction (BHJ), both polymer crystallization and vertical phase segregation contributed to the better device performance, whereas in the inverted BHJ, the concentration gradient remains unchanged after annealing because of the insertion interlayers. Therefore, the increased in inverted device performances is due to the polymer crystallization. The OSC device performance can be further enhanced by inserting interlayer such as poly(3,4-ethylenedioxythiophene) poly(styrenesulfonate) (PEDOT:PSS) which acts as both hole transporting layer and electron blocking layer, and titanium (IV) oxide (TiO_x) which function as electron transporting layer as well as hole blocking layer. These interlayers promoted charge collection, prevent charge recombination and current leakage. To reduce the device fabrication cost, we investigated inverted bulk heterojunction solar cells fabricated with gold (Au) leaf as laminated top electrodes to replace the costly and time consuming vacuum evaporation process. We demonstrated that the Au leaf can be successfully transferred from a supporting polyethylene terephthalate (PET) substrate to the surface of PEDOT:PSS due to sufficiently higher work of adhesion of Au leaf with PEDOT:PSS compared to PET. By optimizing the lamination conditions by increasing the lamination temperature, the contact between the Au leaf and the PEDOT:PSS becomes homogeneous, thus the power conversion efficiency (PCE) improves. Using Naphtho[1,2-c:5,6-c']bis[1,2,5]thiadiazole based polymer as the p-type semiconductor, the PCE reached 5.07%. The laminated devices exhibited excellent stability comparable to that of the evaporated devices. Although silver and alloys leaves are cheaper than Au leaf, they exhibit lower PCE because of the oxidation, thus not suitable materials as an electrode. Vacuum free process not only reduced the waste of materials but also shortened the fabrication time, which lead to the low cost OSC.

Keywords: Organic solar cells, Thermal annealing, Lamination, Work of adhesion, Low cost device

ACKNOWLEDGEMENTS

First of all I would like to express my gratitude to my supervisor, Professor Dr. Hideyuki Murata for his continuous guidance, knowledge, patience and support throughout this research period.

I would like to thank my committee members Associate Professor Dr. Keisuke Ohdaira, Professor Dr. Masahiko Tomitori, Professor Dr. Noriyoshi Matsumi, and Professor Dr. Yutaka Matsuo for the valuable comments.

A special thanks to Dr. Varun Vohra for his generous assistance and contributions during my study. I would like to express my gratitude to Associate Professor Dr. Keisuke Ohdaira for the dark *J-V* simulation, Mr. Koichi Higashimine for the EDS measurements, Dr. Tetsuya Murakami for the XPS measurements, and Dr. William Porzio from ISMAC for the XRD measurements.

Also, thanks to our collaborators Professor Dr. Kazuo Takimiya and Dr. Itaru Osaka from RIKEN for providing the PNTz4T polymer and Dr. Masayuki Kanehara from Okayama University for the Au NPs ink.

For Murata lab members and friends in JAIST, I'm so grateful for the help and support that I have been receiving all this time. Thank you for the wonderful times that we shared together.

Most of all, I am so grateful for the prayers, love and support from my parents and brother. Thanks for always being there when I need the comforting words.

Table of Contents

CHAPTER 1: INTRODUCTION

CHAPTER 2: FABRICATION AND CHARACTERIZATION

CHAPTER 3: FACTORS THAT INFLUENCE THE DEVICE PERFROMANCE

CHAPTER 4: FABRICATION OF ORGANIC SOLAR CELLS DEVICES BY VACUUM FREE PROCESS

CHAPTER 5: CONCLUSIONS AND FUTURE WORKS

CHAPTER 1: INTRODUCTION

1.1 Introduction to solar cells

Nowadays, the demand for electrical energy usage is getting higher, but the energy production is still mainly based on the burning fossil fuels such as coal or petroleum. However, this method has negative effects to the environment and living things such as air pollution and the greenhouse effect. The reserves of the fossil fuels are also decreasing over time. Therefore, the needs for renewable and environmentally friendly energy are inevitable. Solar, wind, geothermal and hydro energy are the major renewable energy resources that can replace fossil fuel energy. Solar energy has several advantages over other types of renewable energies such that it does not need large space to mount the solar cells module and it is safe for the users and the environment as compared to the hydro energy.

There are mainly two types of solar cell that are available, which are inorganic and organic solar cells (OSC). In this chapter, we will briefly introduce inorganic solar cells and the details about OSC including the current research in OSC.

1.1.1 Inorganic solar cells

The first solar cells were patented in 1946 by Ohl.1) Chapin et.al. then obtained power conversion efficiency (PCE) of 6% by implementing a single-crystal silicon (Si) wafer for light absorption and a p-n junction for charge separation.2) The principle of wafer Si solar cells is shown in Fig. 1.0(a), which consists of photo absorption throughout the wafer, and charge separation that often involves diffusion of photo-excited charge carriers. Light absorption in inorganic solar cells leads directly to the creation of free electron-hole pairs.$^{3)}$ The structure and fabrication steps of a single crystalline Si solar cells are shown in Fig. 1.0(b).

Even though crystalline Si solar cells are the most commercially fabricated solar cells, other types of solar cells are also actively developed, for examples, multicrystalline Si, amorphous Si, cadmium telluride (CdTe), copper indium gallium selenide (CIGS) and single-junction gallium arsenide (GaAs).$^{4-5)}$ The PCE of inorganic solar cells is currently up to 27.6% for single concentrator single crystal crystalline Si cells and 44.7% for four junction cells based on III-V compound.$^{6)}$ However, the module is heavy thus makes the installation and shipping cost of inorganic solar cells become expensive, which is the drawback for inorganic solar cells.$^{4)}$

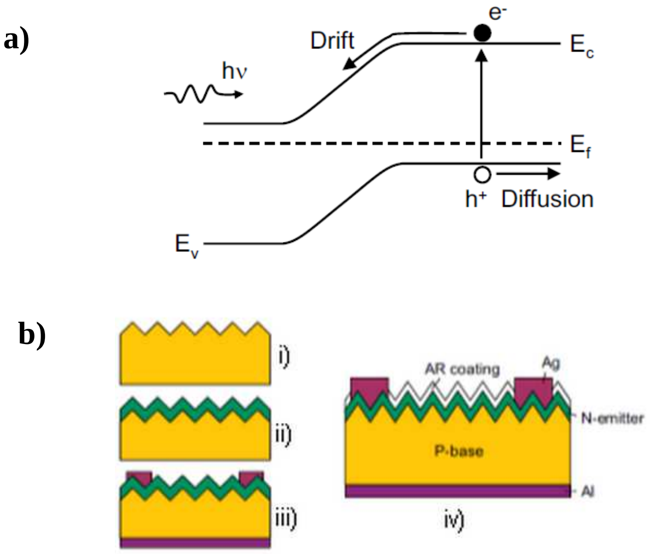

Fig. 1.0: a) Principle of wafer Si solar cells: photon absorption throughout the wafer and charge separation often involves diffusion of photo-excited charge carriers. b) Cross section (iv) and fabrication step of single crystal Si solar cells: (i) surface texturing, (ii) n-emitter diffusion, (iii) metallization, and (iv) antireflection (AR) coating.$^{4)}$

1.1.2 Organic solar cells

The motivation for OSC development is to overcome the cost issue that is faced in the inorganic solar cells, by producing lightweight and solution processable OSC, which will lead to cheaper installation and shipping cost.7) At the same time, many researchers are trying to increase the PCE of OSC device to compete with that of the inorganic ones. Therefore, both high device performance and low production cost must be achieved simultaneously. Initially, the active layers were made from small organic molecules. The first OSC device was based on single organic layer which is sandwiched between two different work function metal electrodes.8-9) However, the PCE was very low, around 10^{-3}% to 10^{-2}%. The PCE able to reach 0.7% by using merocyanine dyes.10)

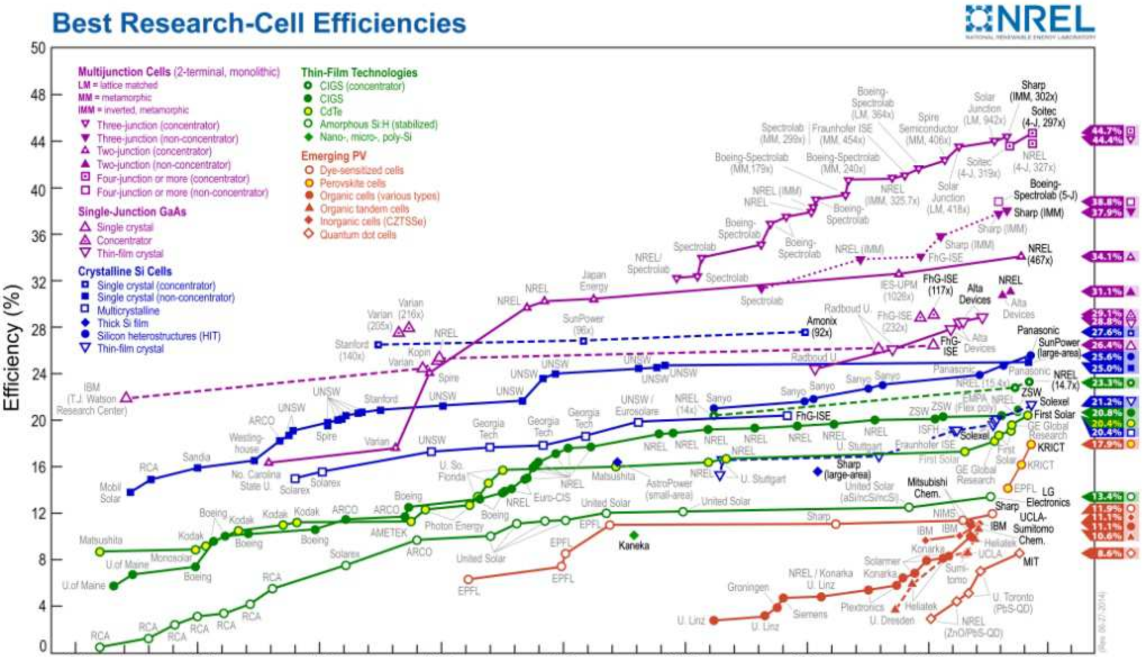

Fig. 1.1: Record for various types of solar cells efficiency.6)

Then, the device performances were continuously improved by changing the device architectures, such as from single layer to bilayer and to bulk heterojunction (BHJ), and also through materials development.11-12) The highest PCE reported for OSC is 11.1% by Mitsubishi Chemicals.6) Currently, hybrid organic-inorganic perovskite solar cells are showing remarkably more than fourfold increase in the device performances from 3.8% to 17.9% of PCE just within 5 years.13)

1.1.2.1 Working principles and mechanism

Energy conversion process has four fundamental steps to convert the incident solar irradiation to electrical current (Fig. 1.2), which are light absorption and generation of exciton, followed by diffusion of the exciton, then exciton dissociation and finally charge transport and collection at the electrodes.14-16) In the first step, light is absorbed by the donor and generates exciton which can be considered as a strong bound electron-hole pair. Next, the exciton diffuses along the polymer chain towards the donor-acceptor interface. If the diffusion length is large enough to reach near the acceptor molecule, then the exciton will dissociate in which the electron will be transferred to the acceptor. The exciton dissociation is not easy because of the strong Coulomb bound between electron-hole pairs. Energetic driving force is required to separate this bound.14) However, the exciton will recombine if they are unable to dissociate during their lifetime. In contrast, in inorganic solar cells, the light absorption leads directly to the creation of free hole-electron pairs.3,9) Finally, after the dissociation, the electron and hole are transported to the cathode and anode, respectively. Larger donor-acceptor interface are is important to provide more probability for the exciton dissociation to take place which can be seen in the bilayer and BHJ OSC.

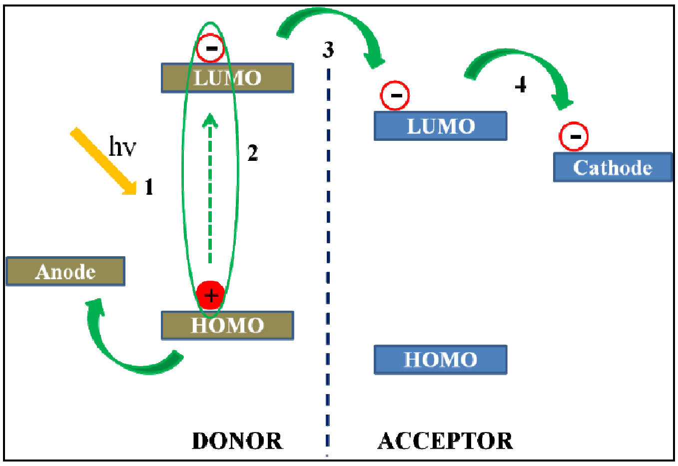

Fig. 1.2: Fundamental steps to convert solar irradiation to electrical current.[14-16)]

1.1.2.2 Bilayer solar cells

The first bilayer OSC device was fabricated by Tang in 1986 which consists of indium tin oxide (ITO)/ copper phthalocyanine (CuPc)/ perylene tetracarboxylic derivative (PV)/ silver (Ag) with PCE about 1%.[17)] The regular structure of bilayer is composed of anode, hole transporting layer (HTL), donor, acceptor, electron transporting layer (ETL) and cathode (Fig. 1.3(a)). It is a type of heterojunction OSC that aims to overcome the issue with low separation of photogenerated charge carriers that faced by the single layer device. In bilayer, the exciton dissociates at the interface between donor and acceptor layer. However, the short exciton diffusion length of organic materials limits the thickness of the donor and acceptor layers. Thick active layer may cause the exciton that generated far from the heterojunction to recombine before arriving at the heterojunction. While thin donor and acceptor layers may cause weak absorption. In bilayer structure, it able to achieve PCE up to 4.40% by using poly(3-hexylthiophene) (P3HT)/ [6,6]-phenyl-C_{61}-butyric acid methyl ester ($PC_{61}BM$) with self-assembled poly(ethylene glycol) modified [60] fullerene (PEGN-C60).[18)]

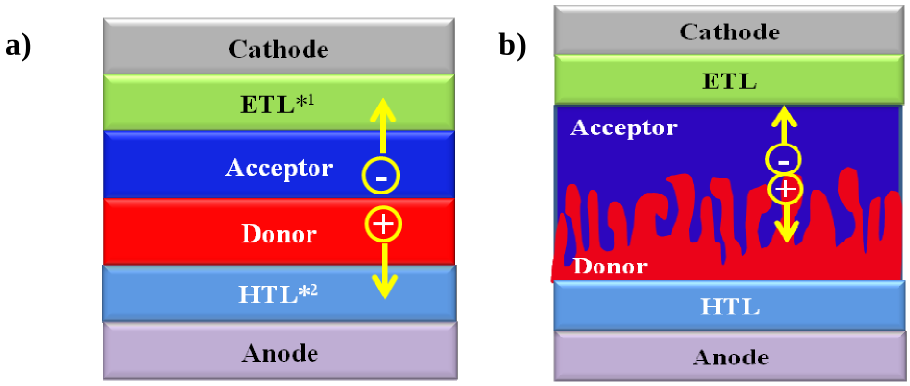

Fig. 1.3: Structure of (a) bilayer and (b) ideal BHJ OSC

1.1.2.3 Bulk heterojunction (BHJ) solar cells

BHJ is successfully formed by mixing donor and acceptor materials in solution and spin coat them to form interpenetrating network film and give more area for exciton dissociation than that of the bilayer. Efficient charge separation which results from photoinduced electron transfer from the donor to acceptor has yields higher PCE than the bilayer.19, 20) This interpenetrating network has increased the dissociation of generated exciton due to the shorter phase separation within the film, which is usually around 10 nm - 20 nm and also the within the exciton length of many organic semiconductors. The shorter phase separation makes it is possible to make a thicker film in BHJ as compared to the bilayer.21)

The polymer:fullerene is the common donor:acceptor materials that are used in BHJ. In addition to an interpenetrating network of donor:acceptor, obtaining correct concentration gradient is also found to contribute to the efficient charge collection. This finding has led to several works to control the morphology of the active layer such as solvent annealing, thermal annealing and adding solvent additives. Selecting an appropriate solvent can increase the device PCE up to threefold as shown by S. E. Shaheen et.al.22) F. Padinger has shown that the PCE can be improved by post-annealing the device above the glass transition temperature of the polymer.23) The device architecture with an ideal concentration gradient of BHJ active layer is shown in Fig. 1.3(b). The highest PCE reported for BHJ OSC is 9.48%, with benzo[1,2-b:4,5-b]dithiophene and thieno[3,4-b]thiophene (TT) copolymers (PBDT-TS1 based polymer) and [6,6]-phenyl-C_{71}-butyric acid methyl ester ($PC_{71}BM$) as the donor and acceptor pairs.24)

1.2 Current research in organic solar cells

Currently, OSC is widely studied by the researchers which are aiming to obtain low cost and comparable device performances to that of the inorganic solar cells. This can be done through donor:acceptor materials development and understand the factors and parameters that contribute to the device performances. At the same time, various fabrication techniques have been explored to realize fully vacuum free fabrication process and towards flexible substrate devices with high throughput production, thus reduce the device fabrication cost.25)

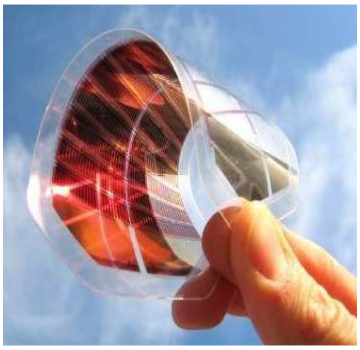

Fig. 1.4: Flexible OSC.26)

Lamination, coating (slot-die coating, knife edge coating), printing (rotary screen printing, screen printing) and spray coating are the examples of technique that can be applied in roll-to-roll process to replace the thermally vacuum evaporation process.[25, 27-29)] Both morphological changes and vacuum free fabrication process are important to obtain efficient, lightweight and cheap OSC device.

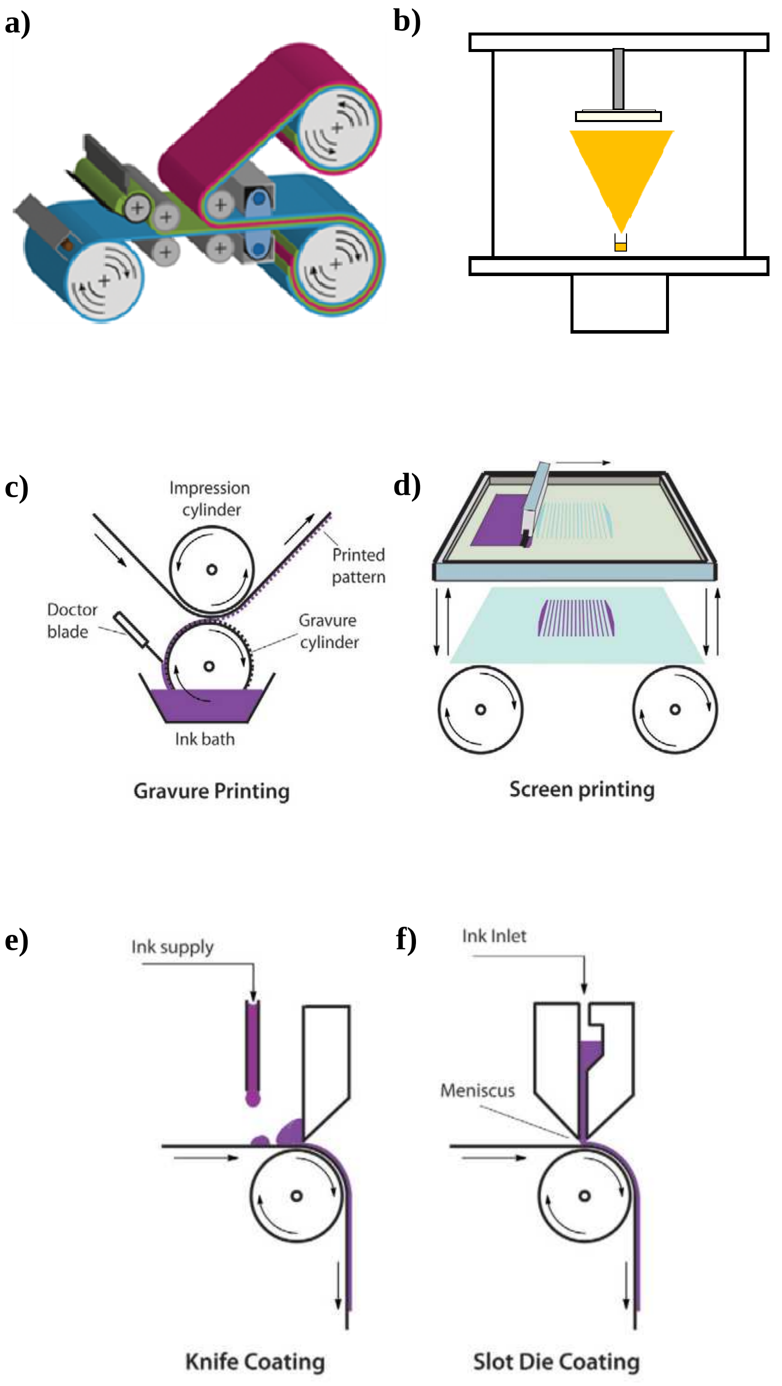

Fig. 1.5: Sketch of: a) lamination process,[30)] b) vacuum evaporation process, c) gravure printing, d) screen printing, e) knife coating, and f) slot die coating.[25)]

1.3 Aims of study

With the motivation to develop efficient and stable device performance, and low cost OSC device, it is important to understand factors that affecting the device performances and to develop fabrication process for low OSC.

Therefore, the aims of this study are: Firstly, to study the factors that contribute to the device efficiency; relationship between thermal annealing and morphology changes in active layer and relationship between interlayer and device performance. Secondly, to fabricate the OSC device by implementing vacuum free top electrode deposition process by gold leaf lamination and gold nanoparticles ink spray coating.

1.4 Structure of this thesis

The body of this thesis comprises of five chapters with two main parts, which are the factors that are affecting to the device performances and fabrication of OSC by vacuum free process. The earlier part is described in Chapter 3, and the later part is described in Chapter 4.

Chapter 1 is focused on the introduction of the organic solar cells. It explained about the OSC operating principles and mechanism, bilayer and BHJ solar cells. It also covered about the current research in OSC, the motivations and aims of this study.

Chapter 2 covered the devices fabrication and characterization. It explained about the materials, device structures and characterization that are used in in this study.

In Chapter 3, the effect of annealing and insertion of interlayer to the device performances are discussed. Upon annealing the regular structure devices, their performances increased because of the polymer crystallization and vertical phase segregation as been observed in the absorption spectra and Energy Dispersive X-ray Spectroscopy (EDS) images. Unlike the regular structure devices, the concentration gradient in the inverted device active layer remains unchanged, which did not in accordance with its ideal concentration gradient. Therefore, the increased in inverted device performances is due to the polymer crystallization. Apart of annealing, the insertion of interlayer to the device structure is found to allow better charge collection and to reduce the leakage current, thus increased the devices PCE.

In Chapter 4, the lamination of gold (Au) leaf is used to replace the vacuum evaporation process, in order to reduce the device fabrication cost. The work of adhesion (*W*) is a useful parameter to select the supporting substrate for Au leaf. With sufficient differences in *W*, the Au leaf is completely transferred from its supporting substrate to the surface of poly(3,4-ethylenedioxythiophene) poly(styrenesulfonate) (PEDOT:PSS). Optimization the lamination temperature exhibited more homogeneous Au leaf coverage on the PEDOT:PSS surface, thus increased the device PCE. The silver (Ag) and alloys leaves which were the candidate materials to further reduce the cost showed lower device performances due to the oxidation. The laminated devices showed comparable stability to that of the evaporated ones, which indicated the good quality of the laminated electrode. The laminated device PCE has increased to 5.0% by using new high performance polymer, Naphtho[1,2-c:5,6-c']bis[1,2,5]thiadiazole (PNTz4T). A cost comparison between using vacuum evaporation and Au leaf lamination as the top electrode are also shown. Besides lamination, we deposited the electrode by spray coating Au nano particles (NPs) ink in the regular structure devices. However, the performances is low and the PCE decrased after annealing due to the increased in Au NPs ink work function upon annealing.

Finally, Chapter 5 summarized the finding from this study and suggested the possible works that can be done in the future that are related to this study.

1.5 References

[1]R. Ohl, U.S. Patent 2, 402,662 (1946)

[2]D. M. Chapin, C. S. Fuller, and G. L. Pearson, J. Appl. Phys. **25**, 676 (1954).

[3]B. A. Gregg and M. C. Hanna, J. Appl. Phys. **93**, 3605-3614 (2003).

[4]M. Tao, The Electrochemical Society Interface, **17**, 30 (Winter 2008).

[5]R. W. Miles, G. Zoppi, and I. Forbes, Mater. Today. **10**, 20 (2007).

[6] http://www.nrel.gov/ncpv/images/efficiency_chart.jpg

[7]J. Nelson, Mater. Today. **14**, 462 (2011).

[8]G.A. Chamberlain, Solar Cells, 8, 47 (1983).

[9]D. Wo¨hrle, and D. Meissner, Adv. Mater. **3**, 129 (1991)

[10]A. K. Ghosh, and T. Feng, J. Appl. Phys, **49**, 5982 (1978).

[11]I. Osaka, M. Shimawaki, H. Mori, I. Doi, E. Miyazaki, T. Koganezawa and K. Takimiya, J. Am. Chem. Soc. **134**, 3498 (2012).

[12]C. Cabanetos, A. E. Labban, J. A. Bartelt, J. D. Doughlas, W. R. Mateker, J. M. J. Fréchet, M. D. McGehee, and P. M. Beaujuge, J. Am. Chem. Soc. **135**, 4656 (2013).

[13]http://www.nrel.gov/news/features/feature_detail.cfm/feature_id=10333

[14]C. Deibel, V. Dyakonov, and C. J. Brabec, IEEE Journal of Selected Topics in Quantum Electronics **16**, 1517 (2010).

[15]B. Thompson and J. Fréchet, Angew. Chem. Int. Ed. **47**, 58 (2008).

[16]G. Chidichimo and L. Filippelli, Int. J. Photoenergy **2010**, 5201 (2010).

[17]C.W. Tang, Appl. Phys. Lett. **48**, 183 (1986).

[18]H. Li,Z. Qi and J. Wang, Appl. Phys. Lett. **102**, 213901 (2013)

[19]G. Yu, J. Gao, J. C. Hummelen, F. Wudl, A. J. Heeger, Science. **270**, 1789 (1995)

[20]F. Yang, M. Shtein and S. R. Forrest, Nat. Mater. **4**, 37 (2005)

[21]D. D. S. Fung, and W. C. H. Choy, *Organic Solar Cells: Materials and Device*

Physics (Springer-Verlag London, 2013) p.9.

[22]S.E. Shaheen, C.J. Brabec, N.S. Sariciftci, F. Padinger, T. Fromherz, and J.C. Hummelen, Appl. Phys. Lett. **78**, 6 (2001).

[23]F. Padinger, R.S. Rittberger, and N.S. Sariciftci, Adv. Funct. Mater. **13**, 85 (2003).

[24]L. Ye, S. Zhang, W. Zhao, H. Yao and J. Hou, Chem. Mater. **26**, 3603 (2014)

[25]R. Søndergaard, M. Hösel, D. Angmo, T. T. Larsen-Olsen and F. C. Krebs, Mater. Today. **15**, 36 (2012).

[26]http://www.solarcontact.com

[27]F. C. Krebs, J. Alstrup, H. Spanggaard, K. Larsen and E. Kold, Sol. Energy Mater. Sol. Cells. **83**, 293 (2004).

[28]F. C. Krebs, Sol. Energy Mater. Sol. Cells. **93**, 465 (2009).

[29]J. K. Kim, W. Kim, D. H. Wang, H. Lee, S. M. Cho, D. G. Choi and J. H. Park, Langmuir. **29**, 5377 (2013).

[30]M. Hösel, R. R. Søndergaard, M. Jørgensen and F. C. Krebs, Adv. Eng. Mater. **15**, 1068 (2013).

CHAPTER 2: FABRICATION AND CHARACTERIZATION

2.1 Introduction

In this chapter, we will briefly describe the materials that are used in solar cell devices fabrication and their properties, device architectures and also the instruments used to characterize the solar cell devices.

2.2 Materials

2.2.1 Donor and acceptor materials

In the BHJ solar cells presented here, p-type polymer and fullerene correspond to the electron donor and acceptor materials, respectively. For this work, we will focus on poly(3-hexylthiophene) (P3HT) and [6,6]-phenyl-C_{61}-butyric acid methyl ester ($PC_{61}BM$) donor:acceptor system The P3HT that we used for regular structure was from Merck, Batch No. EF 430602 with Mw of 20,050 g/mol, and for inverted structure was Sepiolid P200 from BASF, with an average molecular weight (Mw) 20,000 to 30,000 g/mol. The $PC_{61}BM$ was manufactured by Luminescence Technology Corp., Lot No S905-121005, Product No LT-S905 with Mw of 910.88 g/mol. Their chemical structures are shown in Fig 2.0. P3HT has a strong absorption peak with coefficient of up to 10^5 cm^{-1}.1) It also has a high hole mobility up to 0.1 cm^2 V^{-1} s^{-1} in field effect transistor (FET) 2-3) which is almost identical with the electron mobility of PCBM.4) PCBM has a deep LUMO level (4.2 eV) which provide the molecule with a very high electron affinity and induces versatility with respect to the numerous potential organic donors.5) It also has a very high electron mobility up to 0.1 $cm^2 V^{-1} s^{-1}$ in FET.[4] These two materials represent a donor:acceptor reference combination in organic solar cells research 6-7) as they are commercially available 8) and able to achieve high PCE up to 6.8%.9)

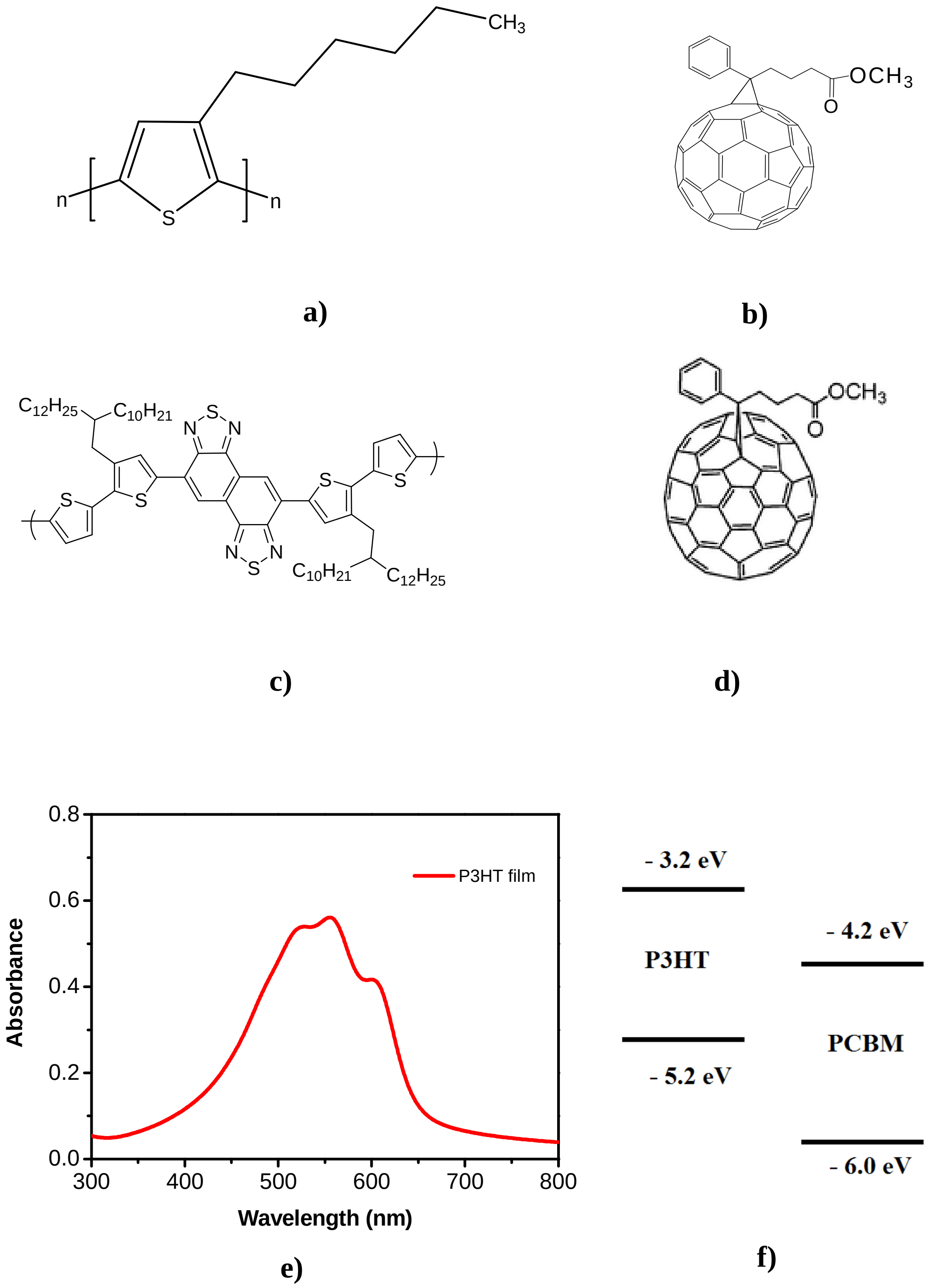

a)

b)

c)

d)

e)

f)

Fig. 2.0: Chemical structures of (a) P3HT, (b) $PC_{61}BM$, (c) PNTz4T and (d) $PC_{71}BM$. (e) Absorption spectra of P3HT and (e) example of HOMO and LUMO level of P3HT and $PC_{61}BM$5)

On top of that, we also used Naphtho[1,2-c:5,6-c']bis[1,2,5]thiadiazole (PNTz4T) and [6,6]-phenyl-C_{71}-butyric acid methyl ester ($PC_{71}BM$) as donor and acceptor materials. PNTz4T has high mobility of ~0.56 $cm^2\ V^{-1}s^{-1}$ in FET, wide absorption up to 800 nm, LUMO of -3.77 eV and relatively low-lying HOMO of -5.2 eV.10) The PNTz4T was provided by Professor Kazuo Takimiya from RIKEN with Batch No. PNTz4T-DT(P2-9) and Mw 52000 g/mol. $PC_{71}BM$ has LUMO at -4.0 eV and HOMO at -6.1 eV.11) It also has higher absorption coefficient at visible region.12) The $PC_{71}BM$ was from Luminescence Technology Corp., Lot No S923-120229 and Product No LT-S923.

2.2.2 Hole transporting layer (HTL)

The HTL that we select is poly(3,4-ethylenedioxythiophene)-poly(styrenesulfonate) also known as PEDOT:PSS. It consists of a polymer, poly(3, 4-ethylenedioxythiophene) (PEDOT) and a water soluble polyelectrolyte, poly(styrenesulfonate) (PSS) as shown in Fig. 2.1. Its high conductivity (ca. 10 S/cm), high visible light transmissivity, water solution processability, insolubility in organic solvents and excellent stability of water soluble polyelectrolyte makes it an ideal interlayer material for solution processed OSC.13) Therefore, it became one of the most widely used material as HTL.14) We use PEDOT:PSS Clevios^{TM} P VP Al 4083 from Heraeus. It is dark blue colour liquid with work function and boiling point approximately at 5.2 eV and 100 ˚C, respectively.

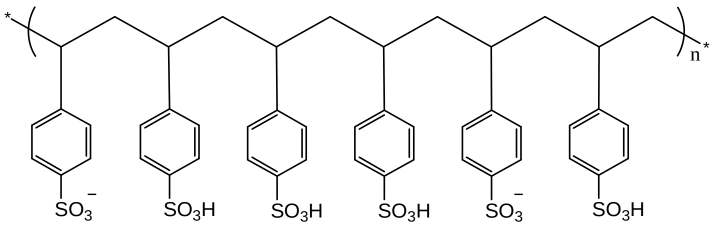

PSS

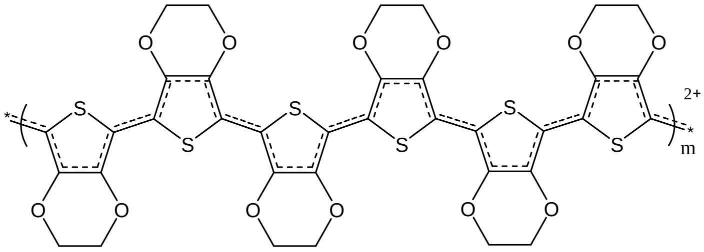

PEDOT

Fig. 2.1: Chemical structures of PSS and PEDOT

2.2.3 Electron transporting layer (ETL)

For the inverted structure BHJ devices, we use titanium (IV) oxide (TiO_x) as an ETL. The chemical bath technique is used to deposit TiO_x layer.$^{15)}$ Cleaned glass/indium tin oxide (ITO) substrates are masked with imide tape to protect the ITO side and the entire rear of the glass side from TiO_x as shown in Fig. 2.2(a). To prepare the TiO_x layer, 0.17 g of hydrogen peroxide (H_2O_2) and 1.60 g of titanium (IV) oxysulfate ($TiOSO_4$) are added into a beaker that is filled with 10 ml pure water. This solution is then transferred into volumetric flask. Pure water is added until the solution becomes 50 ml and mixed well. The solution is then poured into a bottle, and the masked glass/ITO substrates are dipped in it (Fig. 2.2(b)). This bottle is placed into a water bath which is filled with 80 ˚C polyethylene glycol (Fig. 2.2(c)). When the solution started to become cloudy due to the heating, the dipping time of ITO substrates started counting at this point and left for 6 min. After that, the substrates are sonicated in pure water for 10 min. Finally, the substrates are heated on the hot plate for 1 h to form amorphous TiO_x. The thickness is approximately 30 nm. This TiO_x layer shows good stability for unencapsulated inverted BHJ devices by maintaining 94% of the devices stability after 100 h of constant irradiation time (under 1.5 AM).15) Its work function is 4.63 eV, measured using AC2 photoelectron yield spectroscopy.

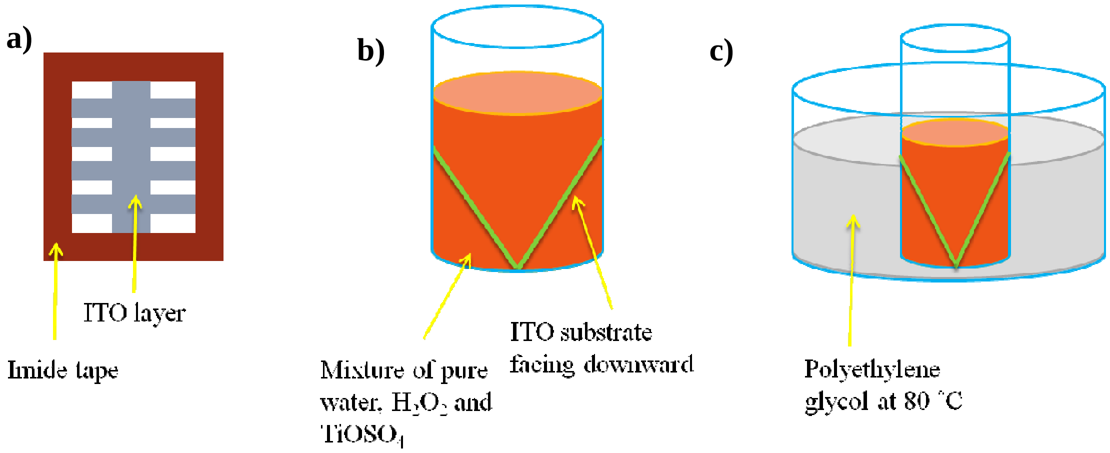

Fig. 2.2: Preparation of chemical bath TiO_x: a) masking the glass/ITO substrate, b) dipping the glass/ITO substrates in the mixture of pure water, H_2O_2 and $TiOSO_4$ solution, and c) deposition of TiO_x layer in 80 ˚C polyethylene glycol.

2.2.4 Au Nanoparticles Ink

In order to go for vacuum free solar cells, we try spray coating of gold (Au) nanoparticles (NPs) as the top electrode in regular BHJ devices. 2,3,11,12,20,21,29,30-octakis[2-(dimethylamino)ethylthio]naphthalocyanine (OTAN) protected Au (OTAN-Au) NPs ink is provided by Dr. Masayuki Kanehara, an Assistant Professor at Okayama University. The chemical structures of OTAN ligand are shown in Fig. 2.3. The size of OTAN-Au NPs and its film conductivity is 14.4 ± 2.3 nm and 6600 S cm^{-1}, respectively.16) The work function of OTAN-Au NPs is 4.30 eV, measured using AC2 photoelectron yield spectroscopy. Further details regarding the synthesis procedures can be obtained in Ref. 16.

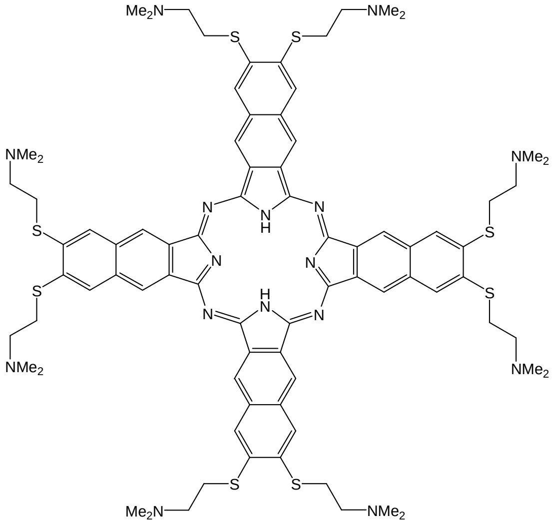

Fig. 2.3: Chemical structures of OTAN ligand

2.2.5 Metal and alloy leaves

Another method to eliminate vacuum evaporation process is using metal leaf as the top electrode in the lamination process. Metal leaf is fabricated based on rolling and pounding. The process starts with rolling the metal into a thin strip, followed by beating the strip into 50-100 µm thick foil. This thin foil is then cut and placed between layers of acetate pieces and pounded until the area increases 4 times. It is then quartered, sandwiched and pounded. These processes are repeated until the metal sheet thickness is reduced to around 100 nm.17) We use pure Au, silver (Ag), Alloy1 (87.5% Au, 12.5% Ag) and Alloy2 (58.69% Au, 41.31% Ag) leaves with the thickness between 100 nm to 150 nm which are bought from Hakuichi Ltd. Fig. 2.4 is an example of an Au (a) and Ag leaves (b).

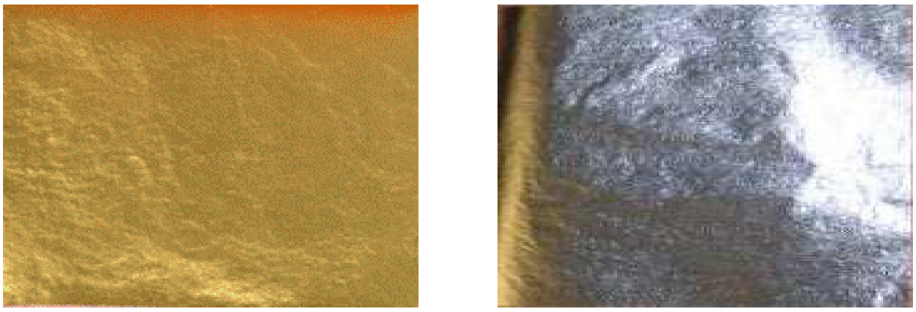

a) **b)**

Fig. 2.4: a) Au leaf and b) Ag leaf

2.3 Structure of bulk heterojunction solar cells

Typically, there are two types of structure of BHJ solar cells, which are regular and inverted structures. The main difference between these two structures is the position of the cathode and anode. As we will see in Chapter 3 and 4 in this research project, both regular and inverted structure solar cell devices were fabricated.

2.3.1 Regular structure

The first BHJ organic solar cell devices were reported in literature by G. Yu et.al., in 1995. They consisted of the following simple regular structure: glass/ ITO (anode)/poly[2-methoxy-5-(2-ethylhexyloxy)-1,4-phenylenevinylene(MEH-PPV):C_{60}/ aluminum (Al) or calcium (Ca) (cathode).18) Since then, many works have been done to optimize the efficiency, including changing the donor:acceptor materials and inserting HTL or ETL.14, 19-20) Our regular devices consist of a glass/ ITO/ PEDOT:PSS/ P3HT:PCBM/ Al layer-by-layer structure, as shown in Fig. 2.5. a). This architecture, referred to as regular structure, corresponds to the devices where the cathode is at the top and the anode is at the bottom.

2.3.2 Inverted structure

In the inverted structure, the anode is at the top and the cathode is the bottom (Fig. 2.5.b). Inverted structure devices have advantages over regular structural devices such as better device stability[15, 23)] where stable metal can be used as top electrode. The evaporation process of top electrode can be replaced with other processes such as the solution process of NPs ink.[24)] These advantages make inverted structure suitable for vacuum free process to reduce the fabrication cost.

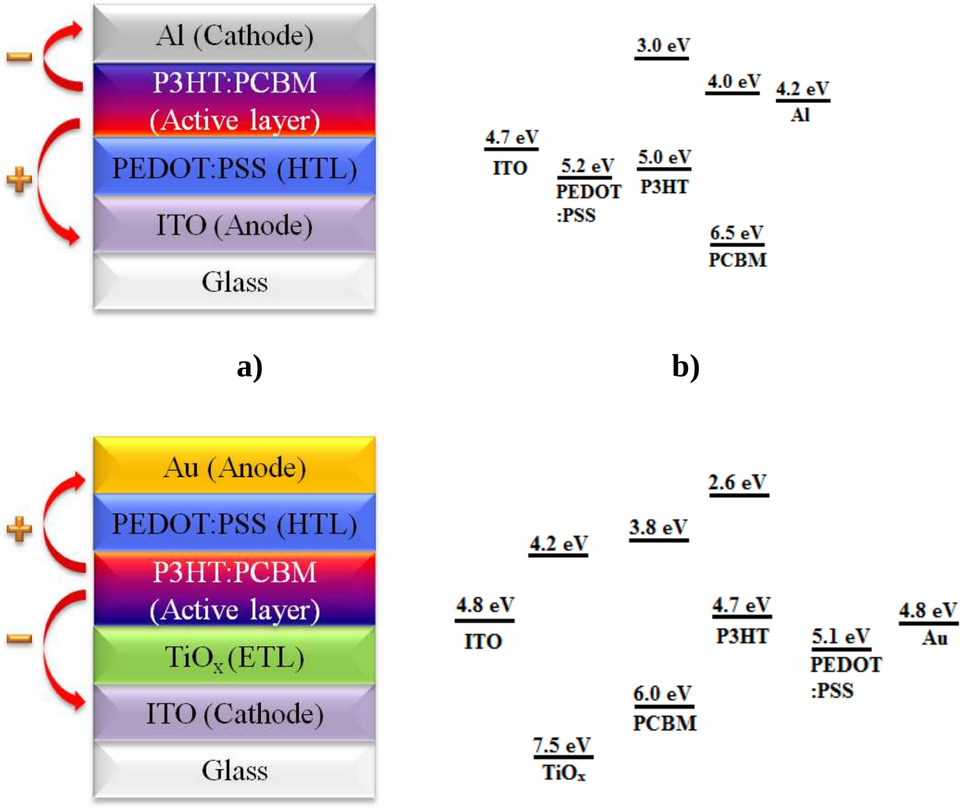

a) b)

c) d)

Fig. 2.5: Schematic diagram of (a) regular structure and (c) inverted structure of OSC, meanwhile (b) and (d) are the examples of the energy diagram for regular[21)] and inverted[22)] structure devices.

2.4 Characterization of solar cell devices

The solar cells PCE are measured using a sourcemeter (2400 Keithley) and a solar simulator at one sunlight irradiance (AM 1.5G, 100 mW/cm^2) at room temperature. Figure 2.6 shows an example of both dark and under irradiation current density-voltage (J-V) curves and how the solar cell parameters can be extracted from such curves. Equation 1 is the equation that is used to calculate the device PCE under irradiation, where P_{out} is output power, P_{in} is input power, J_{max} is maximum current density and V_{max} is maximum voltage. Short circuit current density (J_{sc}) is the current through solar cell when the voltage across the solar cell is zero, open circuit voltage (V_{oc}) is the maximum voltage available from the solar cell when the net current through the device is zero, and fill factor (FF) is a ratio of the maximum power from the solar cell to the product of J_{sc} and V_{oc} (Eq. 2).

Equation 3 is used in dark J-V simulation to obtain reverse saturation current (J_0), ideality factor (n), series resistance (R_s) and shunt resistance (R_{sh}).$^{25, 26)}$ To fit the experimental data to this equation, first convert the experimental J values into ln|J| and then, apply these changes to the both sides of the equation. Finally, use this modified equation for the ln|J|-V curve to obtain the J_0, n, R_s and R_{sh}.

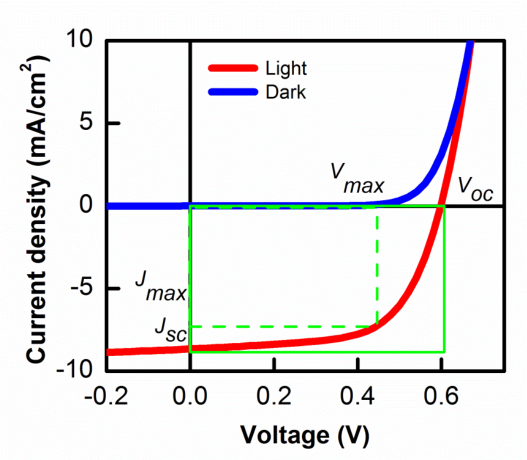

Fig. 2.6: Dark (blue line) and light (red line) J-V curve with the solar cell parameters.

$$PCE = \frac{P_{out}}{P_{in}} \tag{1a}$$

$$PCE = FF\ \frac{(J_{sc})(V_{oc})}{P_{in}} \tag{1b}$$

$$FF = \frac{(J_m)(V_m)}{(J_{sc})(V_{oc})} \tag{2}$$

$$J = J_0\left\{exp\left[\frac{e(V - JR_s)}{nk_BT}\right] - 1\right\} + \frac{(V - JR_s)}{R_{sh}} - J_{ph} \tag{3}$$

2.5 Chapter conclusion

The properties of the materials used in this research work such as P3HT, PCBM, PEDOT:PSS, TiO_x, metal and alloy leaves and Au NPs ink have been briefly described. Regular and inverted structures that we choose for our solar cell devices and the electrical characterization are also presented in this chapter.

2.6 References

[1]U. Zhokhavets, T. Erb, G. Gobsch, M. Al-Ibrahim, and O. Ambacher, Chem. Phys. Lett. **418**, 347 (2006).

[2]H. Sirringhaus, P.J. Brown, R.H. Friend, M.M. Nielsen, K. Bechgaard, B.M.W. Langeveld-Voss, A.J.H. Spiering, R.A.J. Janssen, E.W. Meijer, P. Herwig, and D.M. de Leeuw, Nature **401**, 685 (1999).

[3]C.B. Nielsen and I. McCulloch, Progress in Polymer Science **38**, 2053 (2013).

[4]T.-W. Lee, Y. Byun, B.-W. Koo, I.-N. Kang, Y.-Y. Lyu, C.H. Lee, L. Pu, and S.Y. Lee, Adv. Mater. **17**, 2180 (2005).

[5]B. Thompson and J. Fréchet, Angew. Chem. Int. Ed. **47**, 58 (2008).

[6]B.A. Collins, J.R. Tumbleston, and H. Ade, J. Phys. Chem. Lett. **2**, 3135 (2011).

[7]M.T. Dang, L. Hirsch, and G. Wantz, Adv. Mater. **23**, 3597 (2011).

[8]P.P. Khlyabich, B. Burkhart, A.E. Rudenko, and B.C. Thompson, Polymer, **54**, 5267 (2013).

[9]S.-H. Lee, J.-H. Kim, T.-H. Shim, and J.-G. Park, Electron. Mater. Lett. **5**, 47 (2009).

[10]I. Osaka, M. Shimawaki, H. Mori, I. Doi, E. Miyazaki, T. Koganezawa and K. Takimiya, J. Am. Chem. Soc. **134**, 3498 (2012).

[11]W. W. H. Wong, J. Subbiah, S. R. Puniredd, W. Pisula, D. J. Jones and A. B. Holmes, Polym. Chem., **5**, 1258 (2014).

[12]M. M Wienk, J. M. Kroon, W. J. H. Verhees, J. Knol, J. C. Hummelen, P. A. V. Hal and R. A. J. Janssen, Angew. Chem. **115**, 3493 (2003).

[13]L. Groenendaal, F. Jonas, D. Freitag, H. Pielartzik, and J.R. Reynolds, Adv. Mater. **12**, 481 (2000).

[14]J. Park, T.-W. Lee, B.-D. Chin, D. Wang, and O. Park, Macromol. Rapid Comm. **31**, 2095 (2010).

[15] T. Kuwabara, H. Sugiyama, M. Kuzuba, T. Yamaguchi, and K. Takahashi, Org. Electron. **11**, 1136 (2010).

[16] M. Kanehara, J. Takeya, T. Uemura, H. Murata, K. Takimiya, H. Sekine, and T. Teranishi, B. Chem. Soc. Jpn. **85**, 957 (2012).

[17] Y. Ding, Y. J. Kim and J. Erlebacher, Adv. Mater. **16**, 1897 (2004).

[18] G. Yu, J. Gao, J. C. Hummelen, F. Wudl, A. J. Heeger, Science. **270**, 1789 (1995)

[19] M. Jørgensen, K. Norrman, S. Gevorgyan, T. Tromholt, B. Andreasen, and F. Krebs, Adv. Mater. **24**, 580 (2012).

[20] V. Shrotriya, G. Li, Y. Yao, C.-W. Chu, and Y. Yang, Appl. Phys. Lett. **88**, 253503 (2006).

[21] M. D. Irwin, D. Bruce Buchholz, A. W. Hains, R. P. H. Chang, and T. J. marks, in *Proceedings of the National Academy of Science of The United States of America*, **105**, 2783 (2008).

[22] T. Kuwabara, H. Sugiyama, T. Yamaguchi, and K. Takahashi, Thin Solid Films, **517**, 3766 (2009).

[23] C.S. Kim, S.S. Lee, E.D. Gomez, J.B. Kim, and Y.-L. Loo, Appl. Phys. Lett. **94**, 113302 (2009).

[24] J. Nelson, Mater. Today. **14**, 462 (2011).

[25] A. Orimo, K. Masuda, S. Honda, H. Benten, S. Ito, H. Ohkita, and H. Tsuji, Appl. Phys. Lett. **96**, 043305 (2010).

[26] W. Potscavage, A. Sharma, and B. Kippelen, Accounts Chem. Res. **42**, 1758 (2009).

CHAPTER 3: FACTORS THAT INFLUENCE THE DEVICE PERFORMANCE

3.1 Introduction

To achieve high efficiency OSC devices, it is important to understand the factors that influence the device performances such as control of morphological changes in the active layer and the role of the interlayer. Thermal annealing is one of the methods used to control the morphology of the P3HT:PCBM as thermal annealing induces the polymer crystallization and promotes phase separation1-3). The desired active layer morphology therefore can be achieved through thermal annealing and this has also made the devices PCE remarkably increased by controlling the annealing temperature and time. During annealing process, it is reported that the P3HT polymer chains are reorganized and the crystals grow larger. Meanwhile, this process will diffuse the PCBM molecules into the composite to form aggregates or needle like crystals.4-5) P3HT crystallization leads to a better absorption and yields higher hole mobility which prevents geminate pair recombination. FF at the same time continue to increase slowly due to the increase in carrier mobility.6) Correct concentration gradient of P3HT and PCBM in active layer is desirable for efficient charge collection at the respective electrodes.3,7-9) Therefore, we conducted several experiments to understand the relationship between morphology of the active layer and device parameters.

Several works reported that by inserting a hole or an electron transporting layer, it will improve the hole or electron collection and could prevent the leakage current at the organic/electrode interface. This also will further enhance the devices PCE.10-13) The most commonly used interlayer materials are PEDOT:PSS and metal oxide. 14-16)

3.2 Experimental

3.2.1 Fabrication of inverted structure device

A 45 mg/ml of P3HT:$PC_{61}BM$ solution with 15 mg: 12 mg ratio in 0.6 ml chlorobenzene was prepared and stirred over night at 50 ˚C on the hot plate. The P3HT that we used was Sepiolid P200 from BASF, with an average molecular weight (Mw) 20,000 to 30,000 g/mol, and the $PC_{61}BM$ was manufactured by Luminescence Technology Corp., Lot No S905-121005, Product No LT-S905 with Mw of 910.88 g/mol. Glass ITO/TiO_x substrates were prepared by using the chemical bath technique and annealed at 150 ˚C for 1 h prior to active layer deposition. After filtering with a 0.20 µm 13JP filter from Advantec, the P3HT:PCBM solution was spin coated on top of the TiO_x layer at 700 rpm for 60 s inside the glove box. Next, PEDOT:PSS (Clevios P VP.Al 4083) doped with 0.5 wt% Triton X-100 spin coated at 2000 rpm for 60 s. The devices are finalized by depositing 100 nm thick Au electrodes at a pressure of 10^{-7} torr. These devices were annealed at 150 ˚C for 5 min and subsequently at 70 ˚C for 30 min. The devices were also encapsulated and characterized using a Keithley 2400 Sourcemeter and a solar simulator at one sunlight irradiance (AM 1.5G, 100 mW/cm^2).

3.2.2 Fabrication of regular structure device.

Glass ITO substrates were cleaned using the standard cleaning process as described here: sonication in acetone (5 min), semico clean (10 min), pure water (10 min), isopropyl alcohol (IPA) (10 min), followed by IPA vapour exposure (3 min) and UV ozone treatment (30 min). 30 mg/ml of P3HT:PCBM solution with 1:1 ratio in chlorobenzene was prepared and stirred for 4 h in nitrogen filled glove box. The P3HT (regioregular) used were purchased from Merck, Batch No. EF 430602 with Mw of 20,050 g/mol. The $PC_{61}BM$ was manufactured by Luminescence Technology Corp., Lot No S905-110725, Product No LT-S905 with molecular weight (Mw) of 910.88 g/mol. With 0.1 µm filter (Millex), PEDOT:PSS (Clevios P VP.Al 4083) solution was spin coated on top of the ITO substrate at 1600 rpm for 60 s with a 2 s slope and dried at 200 ˚C for 10 min, resulting in a 75 nm thick layer. The P3HT:PCBM solution was then spin coated at 800 rpm for 60 s with 0.20 µm 13JP filter from Advantec inside the glove box which formed 120 nm thick film. The substrates then pre-annealed at 120 ˚C for 10 min prior to the Al electrodes deposition. After depositing 100 nm Al electrodes, the devices were encapsulated in a nitrogen filled glove box and were measured before and after annealing at 140 ˚C for 10 min. The solar cell characteristics were measured using a Keithley 2400 Sourcemeter and a solar simulator at one sunlight irradiance (AM 1.5G, 100 mW/cm^2). This was done at room temperature.

3.3 Influence of annealing to the device performance.

3.3.1 Photovoltaic characteristics before and after annealing.

Table 3.0 summarizes solar cell characteristics of the regular structure devices before and after annealing at 140 ˚C for 10 min. Upon annealing, all solar cell parameters were improved. More specifically, J_{sc} has increased from 7.57 mA/cm^2 to 7.89 mA/cm^2, V_{oc} also has increased from 0.419 V to 0.565 V, FF has improved from 0.441 to 0.554. This has resulted in a large increase of PCE from 1.40% to 2.47%. Thus, this indicates that annealing plays an important role to achieve optimum PCE of the devices which probably contributed by the polymer crystallization[17-18] and/or vertical phase segregation in the active layer.[3,8] To confirm this, we conducted absorption spectra, X-ray Diffraction (XRD) and Energy Dispersive X-ray Spectroscopy (EDS) measurements.

Table 3.0: Solar cell characteristics of the regular structure devices before and after annealing at 140 ˚C for 10 min

Annealing Condition	**J_{sc} (mA/cm^2)**	**V_{oc} (V)**	**FF**	**PCE (%)**
Before annealing	7.57	0.419	0.441	1.40
After annealing at 140˚C for 10 min	7.89	0.565	0.554	2.47

3.3.2 Crystallization of polymer.

After annealing, an improvement in devices solar cell parameters and PCE was observed. To investigate the changes in the polymer crystallinity, the absorption spectra of the pristine P3HT film and blend P3HT:PCBM film in 1:1 ratio before and after annealing were measured (Fig. 3.0) by using UV/Vis spectrometer JASCO V670. The films were spin coated on the quartz substrates.

Figure 3.0(a) shows the absorption spectra of the blend P3HT:PCBM active layer film before and after annealing, while Fig. 3.0(b) shows the absorption spectra of pure P3HT film and the P3HT spectrum extracted from the blend active layer spectrum after subtracting the PCBM contribution. Absorption spectra of the blend film clearly show two peaks which can be attributed to PCBM (334.5 nm) and P3HT (480.5 - 507 nm).

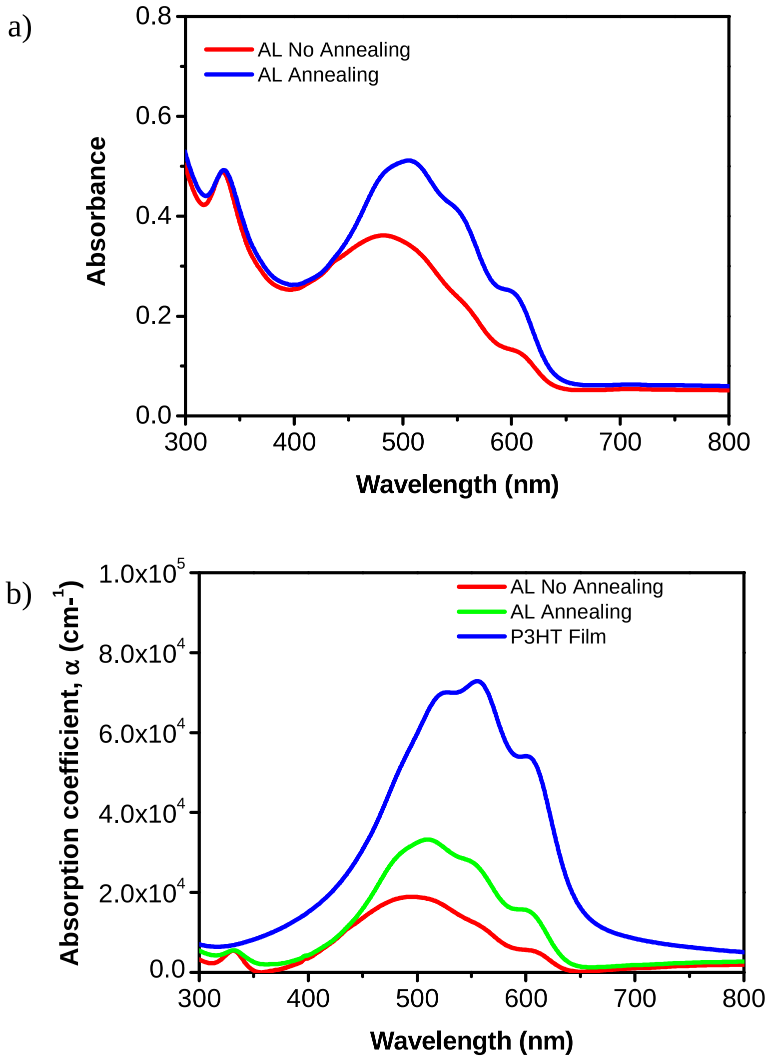

Fig. 3.0: The absorption spectra of (a) of P3HT:PCBM blend film in 1:1 ratio before and after annealing at 140 ˚C for 10 min and (b) absorption spectra of P3HT in blend film before and after annealing after subtracting the PCBM contribution and pristine P3HT film.

After annealing, the peak of PCBM at 334.5 nm and absorption intensity were remain unchanged. However, several changes were observed in the P3HT peak after the annealing such as an induced red-shift of the absorption onset which broadens the spectrum, resulting in an increased light absorption. A vibronic peak appears at 550 nm, a more pronounced shoulder at 606 nm and an increase in absorption intensity can be observed. These are the result of polymer chains self-assemble to form crystallites.4,8) The changes could not be seen before annealing because the finely dispersed PCBM prevented the polymer from forming the crystallites. During annealing, PCBM started to form larger aggregates and at the same time P3HT started to crystallize in the PCBM free regions.19-20) The crystallization of polymers and aggregation of fullerene have resulted in enhanced absorption properties. It is reported that this leads to better charge transport.6) Figure 3.0(b) shows that the blend film spectrum is blue-shifted from the pristine P3HT spectrum. This might originate from a tighter chain due to broken conjugation in the presence of PCBM, which results in shorter conjugated segments and weaker interchain interactions.

The X-ray Diffraction (XRD) data (Fig. 3.1(a)) on the film shows the peak of P3HT at 5.68˚ and 5.60˚ before and after annealing, respectively. The lattice constant, *d*, which are at 1.57 nm before annealing and 1.60 nm after annealing are assigned to the *a*-axis orientation, indicates that the polymer backbone is parallel and the side chain perpendicular to the substrate (Fig. 3.1(b)). After annealing, the intensity of the peak increased and the crystal size also increased from 19 nm to 20 nm. These are the evidence that annealing induced the polymer crystallinity.

The changes in film morphology due to annealing are also observed in AFM images which were taken at 500 nm × 500 nm and 5 µm × 5 µm scale as shown in Fig. 3.2. After annealing, the domains have become larger. The surface roughness (RMS) is on the other hand reduced from 1.54 to 1.28 (5 µm × 5 µm). We assume that these morphological changes are related to the aggregation of the PCBM and crystallization of P3HT.

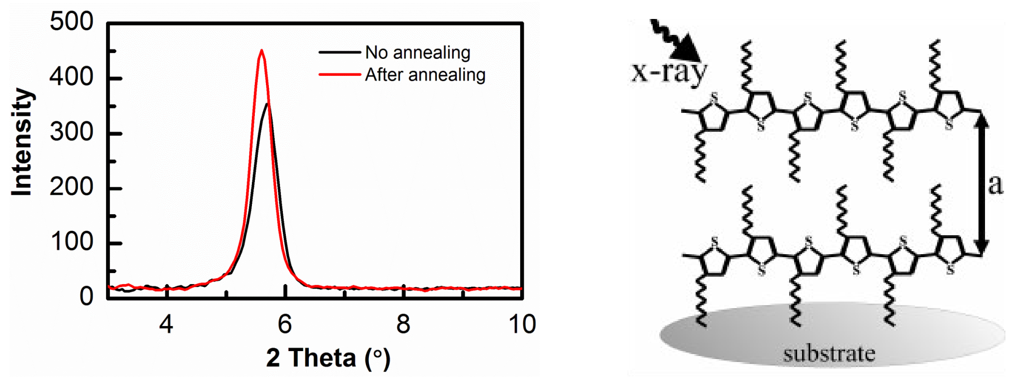

Fig. 3.1: a) XRD spectra of blend film before and after annealing. b) The *a*-axis orientation of the polymer.[20)]

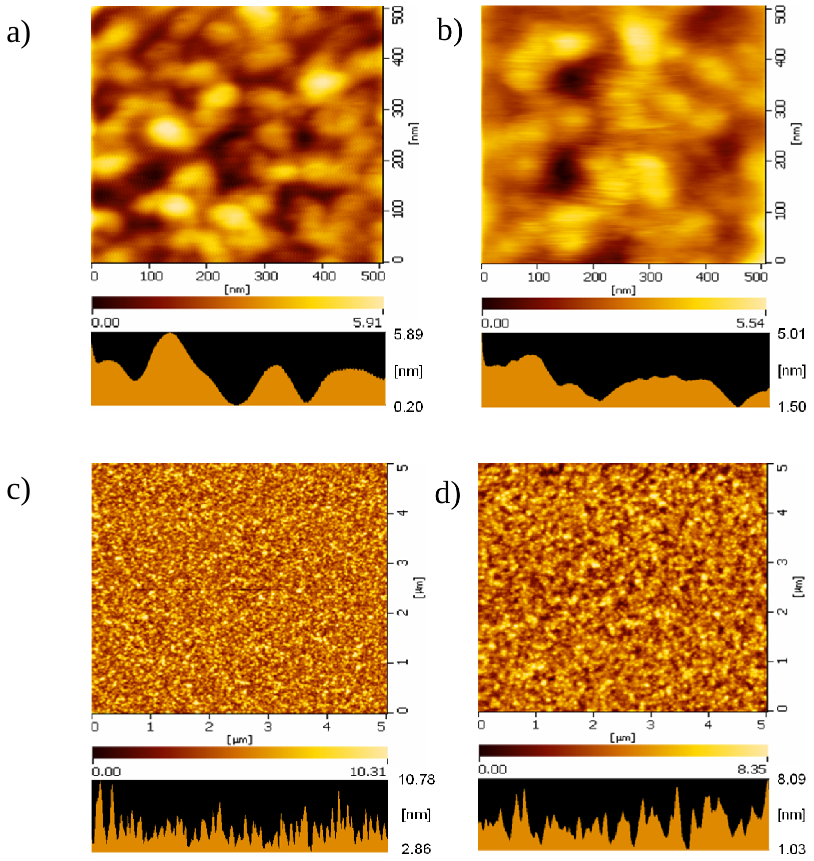

Fig. 3.2: The AFM images of the P3HT:PCBM film a) before annealing and b) after annealing at 500 nm × 500 nm. Meanwhile c) and d) are taken at 5 µm × 5 µm before and after annealing, respectively.

3.3.3 Analysis of the changes in solar cell parameters by using dark *J*-*V* simulation

Regular structure BHJ devices with Al as top electrodes were fabricated. Half of the devices were annealed at 140 ˚C for 10 min and the other half were left unannealed. These devices solar cell parameters were characterized by using the solar simulator and analyzed by using dark *J*-*V* simulation. The *J*-*V* curves and solar cell parameters of the unannealed and annealed devices are shown in Fig. 3.3, and Table 3.1, respectively.

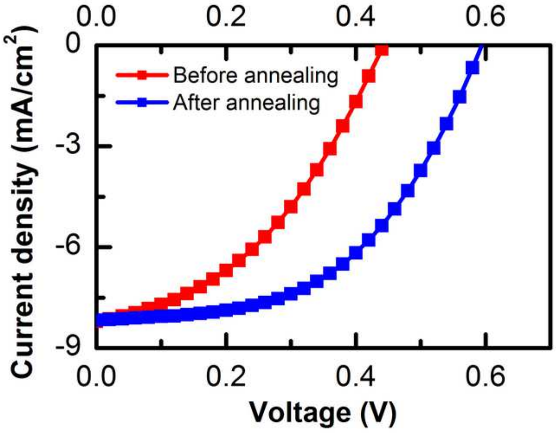

Fig. 3.3: *J*-*V* curves of the regular BHJ devices before and after annealing.

Table 3.1: Summary of solar cell parameters before and after annealing in regular device.

Annealing Condition	**J_{sc} (mA/cm^2)**	**V_{oc} (V)**	**FF**	**PCE (%)**	**J_0 (A/cm^2)**	***n***	**R_s (Ω.cm^2)**	**R_{sh} (Ω.cm^2)**
Before annealing	8.21	0.451	0.401	1.48	6.28×10^{-8}	1.41	68.9	2.78×10^{5}
After annealing	8.17	0.597	0.507	2.47	3.90×10^{-9}	1.61	10.4	8.93×10^{5}

The device shows significant increased in the V_{oc} and FF after annealing. To understand the origin of the V_{oc} and FF increased, the dark *J*-*V* of the unannealed and annealed devices were analyzed using the equivalent circuit model shown in the inset in Fig. 3.4. The dark *J*-*V* curves are fitted very well with the Eq. 3 as shown in Fig.

3.4 and the solar cell parameters are summarized in Table 3.1. R_s is the series resistance, R_{sh} is the shunt resistance, J_0 is the reverse saturation current density, n is the ideality factor, k_B is the Boltzmann constant, e is the elementary charge, A is the active area of the device and T is the temperature.

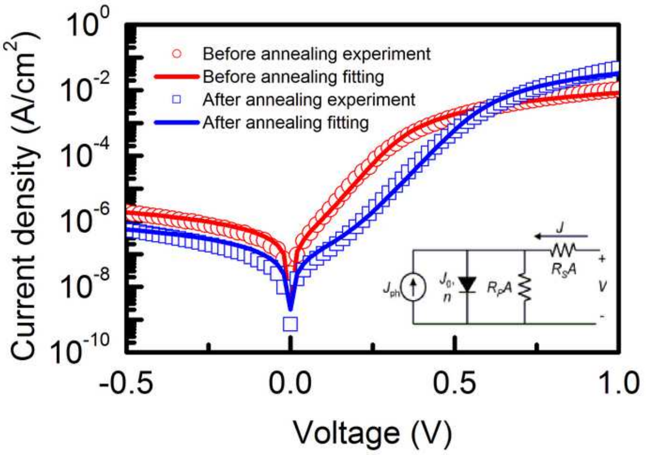

Fig. 3.4: Dark *J*-*V* fitting using the equivalent circuit model as shown in the inset.

Eq. 3 is simplified into Eq. 4 by assuming that J_{ph} is J_{sc} under open circuit conditions and it suggests that small J_0 values will lead to high V_{oc}.[3, 22-23)]

$$J = J_0\left\{\exp\left[\frac{e(V - JR_s)}{nk_BT}\right] - 1\right\} + \frac{(V - JR_s)}{R_{sh}} - J_{ph} \tag{3}$$

$$V_{oc} \approx \frac{nk_BT}{e}\ln\left(\frac{J_{sc}}{J_0}\right) \tag{4}$$

This is in accordance with our results showing that a decrease of almost one order of magnitude of J_0 after annealing resulted in an increase of V_{oc} from 0.451 V to 0.597 V. At the same time, FF and R_{sh} increased while R_s decreased after annealing treatment. These changes are desirable because they indicate better charge collection at the electrode.

3.3.4 Observation of changes in concentration gradient in the regular BHJ

Besides the contribution from the polymer crystallization, another factor that could affect to the morphology changes after annealing is the changes in concentration gradient.3,8) Figure 3.5 represents the ideal concentration gradient in the BHJ film, with P3HT concentrated towards the anode and PCBM concentrated towards the cathode for efficient charge collection.

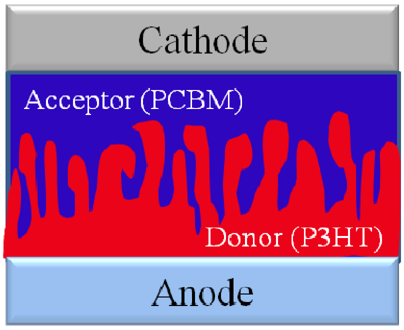

Fig. 3.5: Schematic of ideal BHJ concentration gradient.

To observe the morphological changes in active layer before and after annealing, we analyzed the devices using EDS, which is integrated with Scanning Transmission Electron Microscopy (STEM) to produce elemental mapping at nanometer scale. Regular BHJ structure in horizontal orientation (Fig. 3.6 (a)) is shown to portray similar orientation with the EDS images in Fig. 3.6 (b) and (c). Figure 3.6 (b) and (c) show the EDS elemental mapping with the sulfur intensity, which represents the P3HT intensity in the active layer before and after annealing, respectively. We observed that the intensity of P3HT at the Al interface reduced after annealing and PCBM segregated towards the Al electrode that formed a PCBM rich layer. This PCBM rich layer prevents hole leakage to the Al electrode and resulting in a more efficient charge collection. This contributes to the decreased in J_0, increased in R_{sh} and reduced the R_s respectively.3,19)

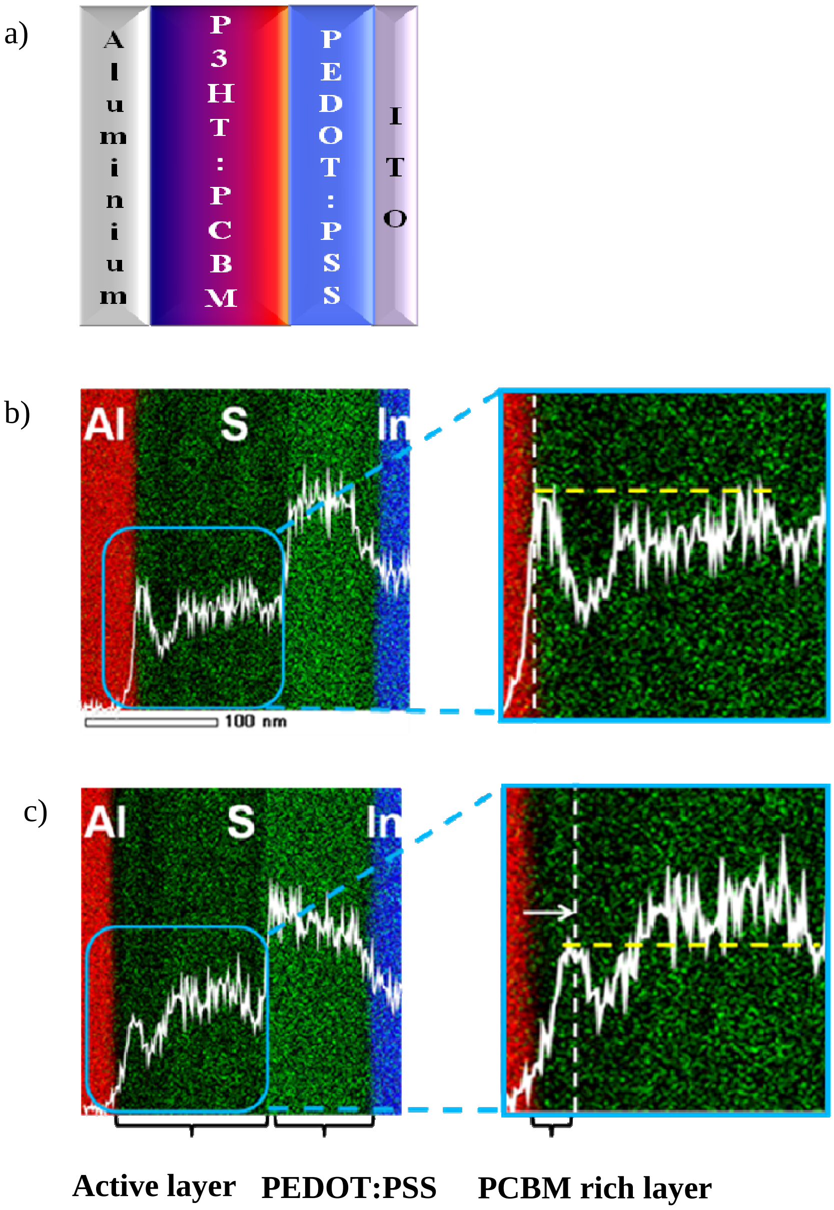

Fig. 3.6: Horizontal representation of the regular BHJ device (a). EDS elemental mapping images with the sulfur intensity (white line), (b) before and (c) after annealing.

3.3.5 Observation on the concentration gradient in the inverted BHJ

The device structure for the inverted BHJ and their *J*-*V* curves before and after annealing are shown in Fig. 3.7 and 3.8, respectively. In the inverted structure devices, the V_{oc} value does not change much before and after annealing, compared to the regular structure device. The high V_{oc} value before annealing is because the insertion of two interlayers (PEDOT:PSS and TiO_x) that reduced the leakage current. J_{sc} and FF have increased from 6.36 mA/cm^2 to 8.63 mA/cm^2, and from 0.329 to 0.626, respectively, which contributed to the increased in device PCE from 1.16% to 3.23% (Table 3.2). From the dark *J*-*V* simulation, we also found that R_s and n decreased, while R_{sh} increased after annealing. Improvement in the solar cell parameters are due to the better charge collection and reduction in charge recombination.20)

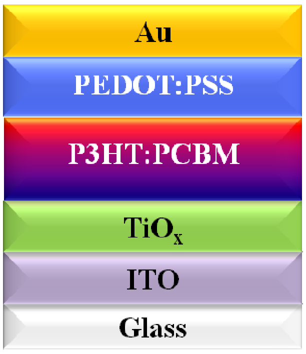

Fig. 3.7: Structure of inverted BHJ device

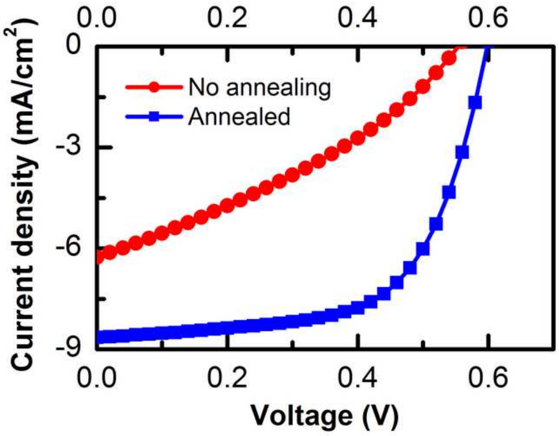

Fig. 3.8: *J*-*V* curves of inverted structure devices before and after annealing.

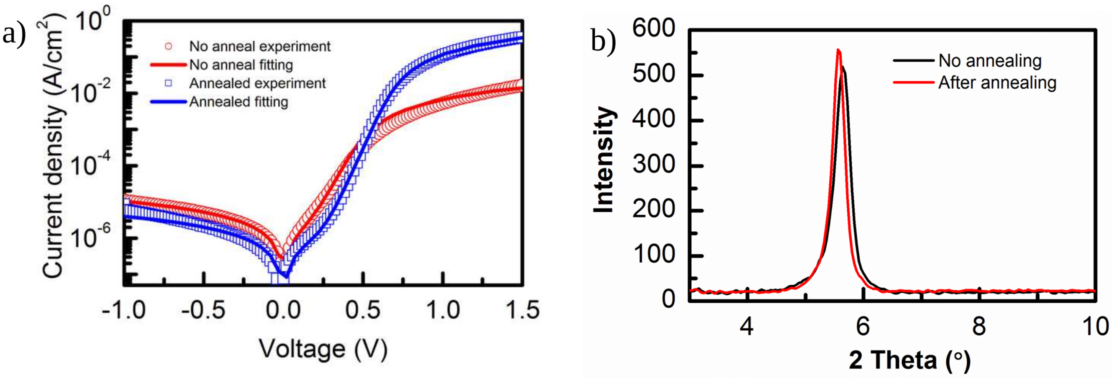

Fig. 3.9: a) Dark *J*-*V* fitting for with and without annealing inverted BHJ devices. b) XRD spectra of the inverted BHJ active layer before and after annealing.

Table 3.2: Summary of solar cell parameters for no annealing and annealed of inverted device.

Annealing condition	J_{sc} (mA/cm^2)	V_{oc} (V)	**FF**	**PCE (%)**	R_s (Ω.cm^2)	R_{sh} (Ω.cm^2)	J_0 (A/cm^2)	n
No annealing	6.36	0.554	0.329	1.16	61.0	9.7×10^4	6.00×10^{-8}	1.99
After annealing	8.63	0.599	0.626	3.23	2.0	2.5×10^5	4.00×10^{-9}	1.75

In the inverted structure device, no significant changes in the sulfur intensity gradient in the active layers were observed before and after annealing, as shown in EDS elemental mapping images in Fig. 3.10. In both Fig 3.10 (c, d), there is a decrease of sulfur intensity (white circle), but this condition is also observed before annealing (Fig. 3.10 (a)). We believe that, the improvement in J_{sc}, FF, R_s and R_{sh} were dominated by the crystallization of polymers instead of vertical phase segregation, as the number of crystals increased after annealing which indicated by the increased of peak intensity in Fig. 3.9(b).

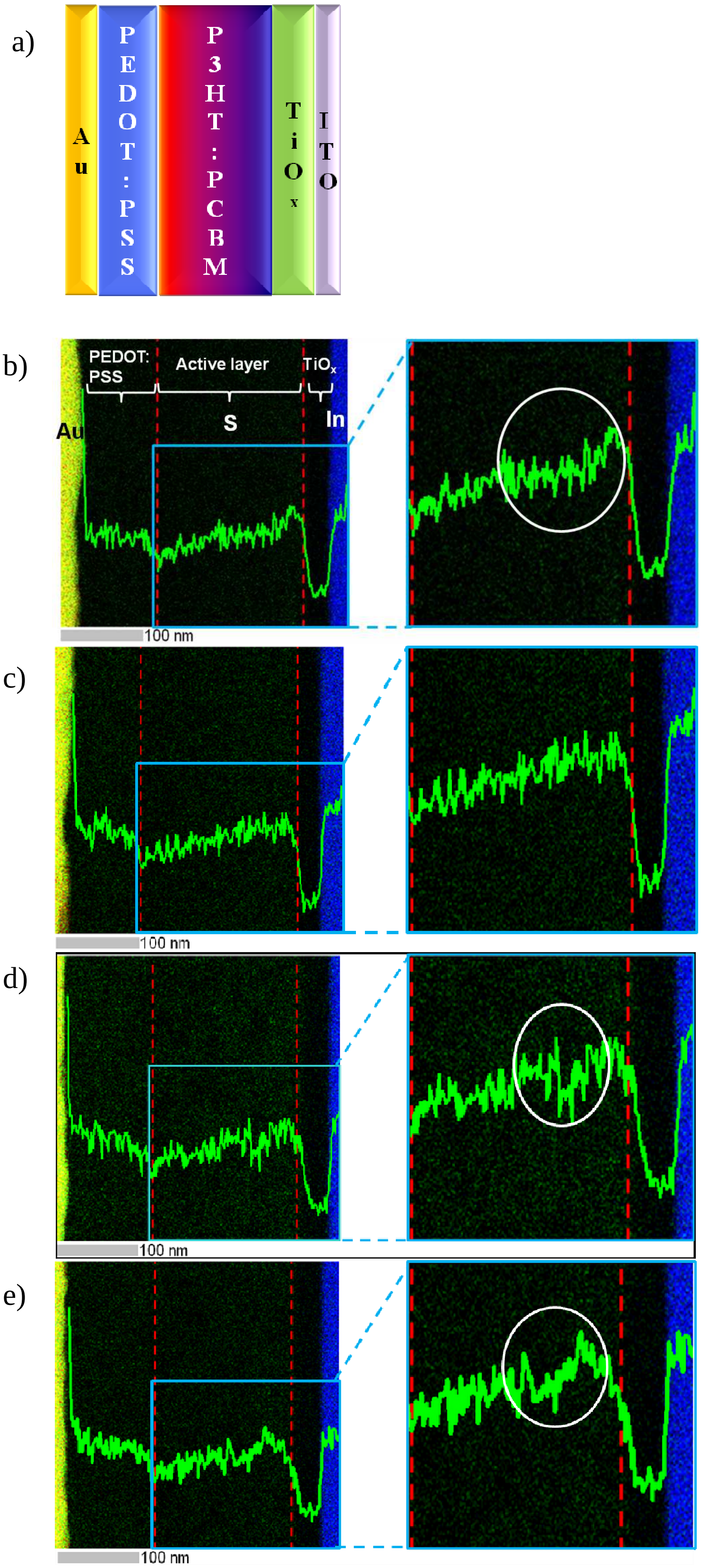

Fig. 3.10: (a) The horizontal representation of the inverted BHJ device. EDS elemental mapping images with the sulfur intensity (green line), (b, c) before and (d, e) after annealing at 150 ˚C for 5 min and subsequently 70 ˚C for 30 min. Two images at different areas are taken from the same device for each annealing conditions.

3.4 Effect of the interlayer insertion to the device performances.

3.4.1 PEDOT:PSS as a hole transporting layer

Fig. 3.11 and 3.12(a) shows the inverted BHJ device structures with and without PEDOT:PSS interlayer, and their *J-V* curves, respectively. Without PEDOT:PSS, the J_{sc}, V_{oc} and FF are 7.31 mA/cm^2, 0.476 V and 0.395, respectively, thus contribute to the 1.38% of PCE. These solar cell parameter values are higher in devices with PEDOT:PSS interlayer, with 8.63 mA/cm^2 of J_{sc}, 0.599 V of V_{oc}, 0.626 of FF and 3.23% of PCE.

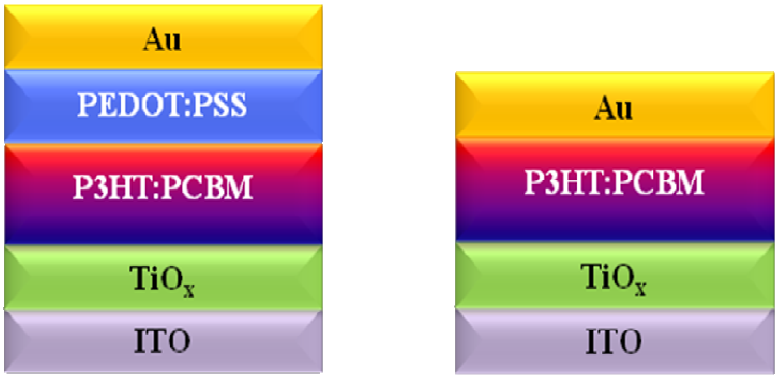

a) b)

Fig. 3.11: Device structure of the inverted BHJ with PEDOT:PSS (a) and without PEDOT:PSS interlayer (b).

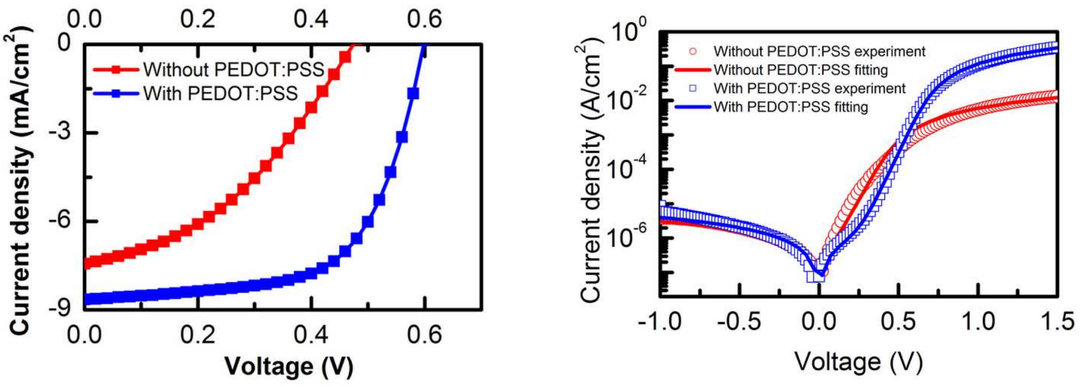

a) b)

Fig. 3.12: (a) *J-V* curves of inverted devices with and without PEDOT:PSS interlayer and (b) dark *J-V* fitting using Eq.3

To further understand PEDOT:PSS contribution to the device performances, we fitted the dark *J*-*V* curves (Fig. 3.12(b)) using Eq.3, and the fitting parameters, R_s, R_{sh}, J_0 and *n* are summarized in Table 3.3.

Table 3.3: Summary of solar cell parameters for devices with and without PEDOT:PSS layer

Devices	**J_{sc} (mA/cm^2)**	**V_{oc} (V)**	**FF**	**PCE (%)**	**R_s (Ω.cm^2)**	**R_{sh} (Ω.cm^2)**	**J_0 (A/cm^2)**	***n***
Without PEDOT:PSS	7.31	0.476	0.395	1.38	73.0	3.3×10^{5}	8.50×10^{-8}	1.98
With PEDOT:PSS	8.63	0.599	0.626	3.23	2.0	2.5×10^{5}	4.00×10^{-9}	1.75

With PEDOT:PSS, the R_s and *n* were improved from 83.0 Ω.cm^2 to 2.5 Ω.cm^2 and from 1.99 to 1.55, respectively. This indicates that the increased in FF on the devices with PEDOT:PSS layer is due to the better hole collection at the top electrode and reduces the charge recombination.[10,13)] The J_0 is reduced from 8.50×10^{-8} to 4.00×10^{-9} contributes to the higher V_{oc} due to the reduction in leakage current. Therefore, PEDOT:PSS interlayer is functioning as HTL and also as electron blocking layer which enhances the overall devices performances, and prevent charge recombination.

3.4.2 TiO_x as an electron transporting layer

Inverted BHJ devices with and without TiO_x interlayer were fabricated (Fig. 3.13) and their *J*-*V* curves are shown in Fig.3.14(a). As compared to the devices without TiO_x interlayer, devices with TiO_x interlayer exhibit better solar cell parameters. J_{sc} has increased from 7.63 mA/cm^2 to 8.63 mA/cm^2, V_{oc} has enhanced from 0.483 V to 0.599 V, FF has improved from 0.491 to 0.626, thus these contributed to the increase in the PCE from 1.81% to 3.23% (Table 3.4).

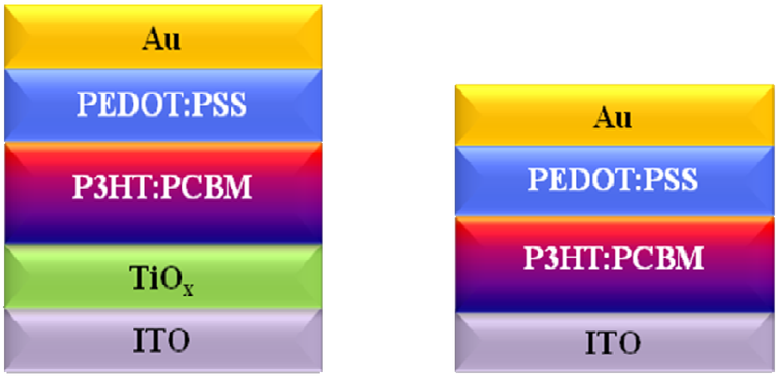

a) b)

Fig. 3.13: Device structure of the inverted BHJ with TiO$_x$ (a) and without TiO$_x$ interlayer (b).

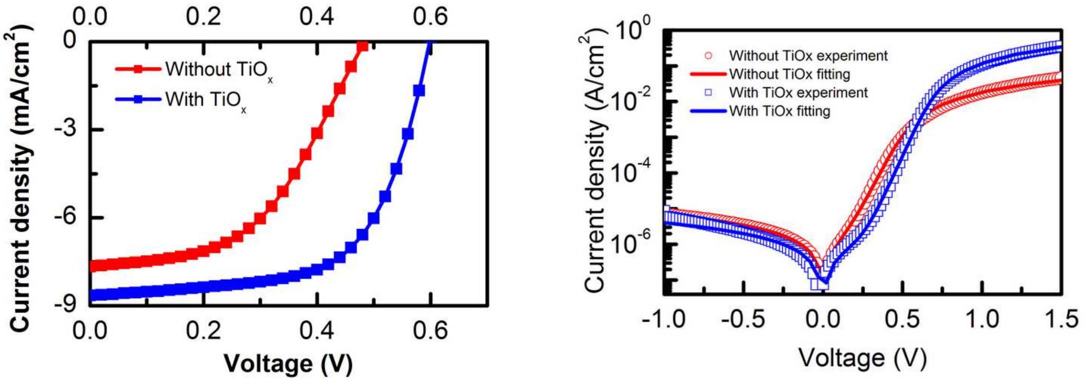

a) b)

Fig. 3.14: (a) *J-V* curves of inverted devices with and without TiO$_x$ interlayer and (b) dark *J-V* fitting using Eq.3

The dark *J-V* curves are fitted by using Eq.3 (Fig. 3.14(b)) and the obtained fitting parameters are summarized in Table 3.4. R_s, and n, were decreased from 21.1 Ω.cm^2 to 2.0 Ω.cm^2, and from 1.96 to 1.75, respectively when TiO$_x$ layer was inserted between ITO and active layer. This indicates that by inserting TiO$_x$, the electron is collected efficiently and it reduced the charge recombination, resulting in higher FF and J_{sc}.[11, 24) The increased in V_{oc} values is due to the decreased in J_0 and increased in R_{sh} values which reduced the leakage current and indicated that TiO_x layer become hole blocking layer.[22) Based on the results, the device performances are improved because of TiO_x layer that acts as both ETL and hole blocking layer, and prevent charge recombination.

Table 3.4: Comparison in PV parameters between devices with and without TiO_x layer

Devices	**J_{sc} (mA/cm^2)**	**V_{oc} (V)**	**FF**	**PCE (%)**	**R_s (Ω.cm^2)**	**R_{sh} (Ω.cm^2)**	**J_0 (A/cm^2)**	**n**
Without TiO_x	7.63	0.483	0.491	1.81	21.1	1.5×10^5	7.60×10^{-8}	1.96
With TiOx	8.63	0.599	0.626	3.23	2.0	2.5×10^5	4.00×10^{-9}	1.75

3.5 Chapter conclusion

In summary, we found that the efficiency of the BHJ solar cells increased significantly after post-annealing. We observed that annealing changes the morphology of the active layer through polymer crystallization and may induce vertical phase segregation. In regular structure device, both polymer crystallization and vertical phase segregation contributed to the increased in V_{oc}, FF, and R_{sh}, and decreased in R_s, which resulted in reduced of leak current and better charge collection. As for inverted structure devices, the improvement in the device performances after annealing is dominated by the polymer crystallization rather than vertical phase segregation. The overall improvement of solar cell parameters increased the device PCE. Therefore, it is crucial to control the morphology of the active layer in order to increase the device performance. Interlayer such as PEDOT:PSS and TiO_x also contribute to the improvement in the device performances. These interlayers do not only act as charge transporting layer but also act as blocking layer, which lead to better charge collection, prevent charge recombination and leak current.

3.6 References

[1] H. Cheun, J.D. Berrigan, Y. Zhou, M. Fenoll, J. Shim, C. Fuentes-Hernandez, K.H. Sandhage, and B. Kippelen, Energy Environ. Sci. **4**, 3456 (2011).

[2] L.-M. Chen, Z. Hong, G. Li, and Y. Yang, Adv. Mater. **21**, 1434 (2009).

[3] A. Orimo, K. Masuda, S. Honda, H. Benten, S. Ito, H. Ohkita, and H. Tsuji, Appl. Phys. Lett. **96**, 043305 (2010).

[4] B. Thompson and J. Fréchet, Angew. Chem. Int. Ed. **47**, 58 (2008).

[5] T.Wang, A.J.Pearson, D.G.Lidzey and R.A.L.Jones, Adv. Funct. Mater. **21**, 1383 (2011).

[6] M.R.Reyes, K.Kim and D.L.Carroll, Appl. Phys. Lett. **87**, 083506 (2005).

[7] Z. Xu, L.-M. Chen, G. Yang, C.-H. Huang, J. Hou, Y. Wu, G. Li, C.-S. Hsu, and Y. Yang, Adv. Funct. Mater. **19**, 1227 (2009).

[8] M. Campoy-Quiles, T. Ferenczi, T. Agostinelli, P. Etchegoin, Y. Kim, T. Anthopoulos, P. Stavrinou, D. Bradley, and J. Nelson, Nat. Mater. **7**, 158 (2008).

[9] V. Vohra, G. Arrighetti, L. Barba, K. Higashimine, W. Porzio, and H. Murata, J. Phys. Chem. Letters **3**, 1820 (2012).

[10] M. Nakamura, C. Yang, K. Tajima and K. Hashimoto, Sol. Energy Mater. Sol. Cells. **93**, 1681 (2009).

[11] J. K. Kim, W. Kim, D. H. Wang, H. Lee, S. M. Cho, D. G. Choi and J. H. Park, Langmuir. **29**, 5377 (2013).

[12] J.-S. Huang, C.-Y. Chou, M.-Y. Liu, K.-H. Tsai, W.-H. Lin, and C.-F. Lin, Org. Electron. **10**, 1060 (2009).

[13] C.-Y. Kuo, M.-S. Su, Y.-C. Hsu, H.-N. Lin, and K.-H. Wei, Adv. Funct. Mater. **20**, 3555 (2010).

[14]J. Park, T.-W. Lee, B.-D. Chin, D. Wang, and O. Park, Macromol. Rapid Comm. **31**, 2095 (2010).

[15]M. Jørgensen, K. Norrman, S. Gevorgyan, T. Tromholt, B. Andreasen, and F. Krebs, Adv. Mater. **24**, 580 (2012).

[16]V. Shrotriya, G. Li, Y. Yao, C.-W. Chu, and Y. Yang, Appl. Phys. Lett. **88**, 253503 (2006).

[17] B. Xue, B. Vaughan, C.-H. Poh, K. B. Burke, L. Thomsen, A. Stapleton, X. Zhou, G. W. Bryant, W. Belcher, and P. C. Dastoor, J. Phys. Chem. C, **114**, 15797 (2010).

[18]P.G. Karagiannidis, S. Kassavetis, C. Pitsalidis, S. Logothetidis, Thin Solid Films, **519**, 4105 (2011).

[19]V.D. Mihailetchi, H.X. Xie, B. de Boer, L.J.A. Koster, and P.W.M. Blom, Adv. Funct. Mater. **16**, 699 (2006).

[20]T. Erb, U. Zhokhavets, G. Gobsch, S. Raleva, B. Stühn, P. Schilinsky, C. Waldauf, and C.J. Brabec, Adv. Funct. Mater. **15**, 1193 (2005).

[21]U. Zhokhavets, T. Erb, H. Hoppe, G. Gobsch, N. S. Sariciftci, Thin Solid Films, **496**, 679 (2006).

[22]N. Li, B.E. Lassiter, R.R. Lunt, G. Wei, and S.R. Forrest, Appl. Phys. Lett. **94**, 023307 (2009).

[23]W. Potscavage, A. Sharma, and B. Kippelen, Accounts Chem. Res. **42**, 1758 (2009).

[24]A. Hayakawa, O. Yoshikawa, T. Fujieda, K. Uehara, and S. Yoshikawa, Appl. Phys. Lett. **90**, 163517 (2007).

CHAPTER 4: FABRICATION OF ORGANIC SOLAR CELLS DEVICES BY VACUUM FREE PROCESS

4.1 Introduction

In the solar cells industry, inorganic devices are still leading in terms of PCE when compared to the OSC. However, due to the high manufacturing cost of inorganic devices, more researchers and industries are shifting towards OSC which could overcome this issue by using solution processes.[1-2)] For instance, OSC offers high throughput manufacturing based on a continuous roll-to-roll process, where the costly metal electrode deposition process could be replaced by other processes such as a lamination.[3-6)] Previously, a study of the metal electrodes lamination for OSCs was conducted in regular BHJ solar cells with Al and Ca as top electrodes. However the device performances were rather low as the electrodes were easily oxidized.[7)] Recently, air stable inverted devices were successfully fabricated through lamination,[2, 8-12)] using more stable metals such as Au as the top electrode[11)] with the highest PCE reported reaching 4.0%.[8)] Furthermore, unlike vacuum evaporation, which induces penetration of metal particles inside the underlying layers, damages to the active layer can be avoided by using the metal electrodes lamination.[13)] In literature, there are two types of lamination approaches have been reported. The first approach is to evaporate the metal on other substrates followed by lamination, where the purpose of the lamination is to prevent damage to the active layer through direct evaporation.[11-12)] While this method still requires vacuum evaporation of metal, the second method completely eliminates it by depositing the electrode on a substrate using a solution process, which will then be laminated.[2,10)] However, such solution processed electrodes require elaborated chemistry to prepare a stable metal dispersion and a careful control over solution deposition conditions to obtain continuous metallic films. Some works to deposit electrode by spray coating high conductivity PEDOT:PSS[14)] and Ag NPs[15)] were also reported.

Recent studies show that laminated devices can be realized by improving adhesion at the interface between two substrates through controlling the surface free energy by irradiating UV light[16-17)] and by adding surfactants into PEDOT:PSS.[10-12)] Despite the improvements of the PCE in laminated devices through process engineering, there is a lack of quantitative explanations to describe on how one can control the transfer and the adhesion of the laminated electrode. A study using double cantilever beam test is used to quantify the fracture energy of the interlayer adhesion between a laminated electrode and an organic layer.[18)] However, this method can only be performed after completing the devices and therefore, it does not allow material selection or lamination efficiency predictions prior to device fabrication.

In this chapter, we will demonstrate vacuum free top electrode deposition process by using metal leaves lamination process. We also will show our attempt to deposit top electrode using spray coating of Au ink NPs.

4.2 Experimental of inverted BHJ devices

4.2.1 Fabrication of inverted BHJ devices

As shown in Fig. 4.0 (a), the devices are prepared with the following architecture: glass substrate/ITO/TiO_x/active layer /PEDOT:PSS with Triton X-100/Au, Ag or alloys. TiO_x films were obtained by following the chemical bath preparation technique.[19)] A P3HT:$PC_{61}BM$ solution (25:20 mg/ml in chlorobenzene) or PNTz4T:$PC_{71}BM$ solution (6:12 mg/ml in dichlorobenzene) were spin coated on top of the TiO_x film as the active layer. PEDOT: PSS was then spin-coated using Triton X-100 as an additive, which is a non-ionic surfactant that allows for PEDOT:PSS to wet and form a continuous layer on top of the organic active layers. For control devices, the electrodes were deposited by vacuum evaporation at the pressure of 9×10^{-7} Torr. For laminated devices, we used a commercially available pure Au leaf (> 99.95%). The Au leaf supported by polyethylene terephthalate (PET) is placed on top of the PEDOT:PSS film and rolled through the lamination machine at a roller speed of 1.5 rpm, a temperature between 100 ˚C to 150 ˚C and with an applied pressure of 0.1 MPa in air (Fig. 4(b)). The time required to form the Au electrodes by the lamination was only 5 min. After metal electrode deposition, both evaporated and laminated P3HT:$PC_{61}BM$ devices were post-annealed at 150 ˚C for 5 min and subsequently at 70 ˚C for 30 min. In the case of PNTz4T:$PC_{71}BM$ devices, the lamination of Au leaf was carried out at 130 ˚C and both laminated and evaporated PNTz4T:$PC_{71}BM$ devices were not subject to the post-annealing because we observed the degradation of the device performance at higher lamination temperature >130 ˚C or by post-annealing after electrode deposition.

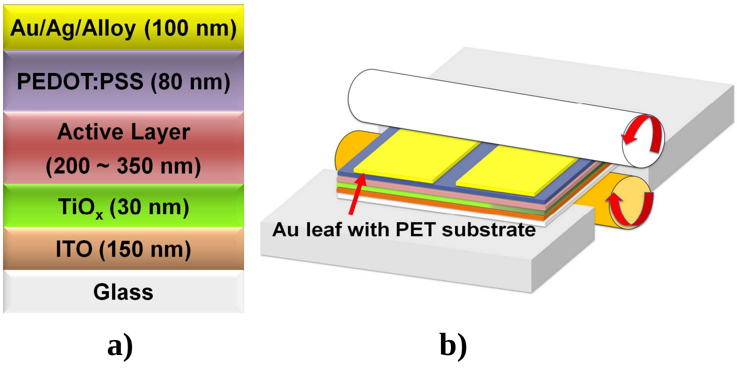

Fig. 4.0: Schematic representation of (a) inverted device architecture and (b) lamination process.

4.2.2 Calculation of work of adhesion

The calculation of work of adhesion (*W*) was applied to select the suitable supporting substrate (PET or polyvinylidene (PVdC)) for the fragile and brittle fracture Au leaf.$^{20)}$ The *W* between Au/PEDOT:PSS should be stronger than that of the Au/PET or Au/PVdC to enable the successful transfer of the Au leaf to the PEDOT:PSS surface. Figure 4.1 shows an example of a condition when the *W* between Au/PEDOT:PSS higher than that of the Au/supporting substrate. These calculations can be completed prior to the device fabrication to select the appropriate materials as a supporting substrate.

Fig. 4.1: Condition when the *W* between Au/PEDOT:PSS higher than the *W* between Au/supporting substrate.

To calculate *W*, we first find the total surface free energy for each of the solid (film and substrates) surfaces (γ_s) which was obtained through the contact angle (θ) measurement. The contact angle measurement was conducted on the various solid surfaces with a selection of measuring liquids (chlorobenzene, chloroform, dichloromethane and benzaldehyde) using an optical tensiometer. Applying Owens and Wendt equation (eq. 5)$^{21)}$ to the four solvents system, we extrapolated the γ_s as described below:

$$\frac{\gamma_l\left(1+\cos\theta\right)}{2\sqrt{\gamma_l{}^d}}=\sqrt{\gamma_s{}^p}\left(\frac{\sqrt{\gamma_l{}^p}}{\sqrt{\gamma_l{}^d}}\right)+\sqrt{\gamma_s{}^d} \tag{5}$$

Equation 5 correlates the various components of the surface free energy (γ) with the θ between the solid surface and the measuring liquid. The polar and dispersive components of γ are represented by the γ^p and γ^d, and the total γ is the sum of them (γ^p + γ^d). The γ_s and γ_l correspond to the surface free energies of the solid and measuring liquid, respectively. The values for $\gamma_l{}^p$ and $\gamma_l{}^d$ of the four solvents were taken from the measuring equipment database and correspond to the values found in literature. By plotting the graph of $\frac{\gamma_l\left(1+\cos\theta\right)}{2\sqrt{\gamma_l{}^d}}$ versus $\left(\frac{\sqrt{\gamma_l{}^p}}{\sqrt{\gamma_l{}^d}}\right)$, $\gamma_s{}^d$ and $\gamma_s{}^p$ values can be extracted, and then the γ_s can be calculated as the sum of these values.

$$\gamma_{Au/sub}=\gamma_{Au}+\gamma_{sub}-2\sqrt{\left(\gamma_{Au}{}^d\gamma_{sub}{}^d\right)}-2\sqrt{\left(\gamma_{Au}{}^p\gamma_{sub}{}^p\right)} \tag{6}$$

$$W_{Au/sub}=\gamma_{Au}+\gamma_{sub}-\gamma_{Au/sub} \tag{7}$$

Once the values for the γ_s of all films and substrates were obtained, the interfacial energy values between Au leaf with PEDOT:PSS, PVdC or PET substrates (sub), $(\gamma_{Au/sub})$ were calculated through eq. 6. Finally, we obtained the W between Au leaf with PEDOT:PSS, PVdC and PET substrates $(W_{Au/sub})$ by applying eq. 7.

4.2.3 Characterization of inverted BHJ devices

The PV characteristics of the devices were measured using a sourcemeter (Keithley 2400) and a solar simulator (AM 1.5G, 100 mW/cm^2) at room temperature. The active area for the evaporated devices is ranging between 0.02 to 0.04 cm^2, and for the laminated devices, the active area is 0.1 cm^2. The optical microscope images of the electrodes were taken by using Keyence VN-8000 nanoscale hybrid microscope. X-ray photoelectron spectroscopy (XPS) was used to measure the surface analysis of the metal and alloy leaves.

4.3 Lamination of metal leaves as top electrode

4.3.1 Importance of work adhesion in lamination process

From eq. 5, we found that the γ_s of Au leaf, PEDOT:PSS, PVdC and PET substrate are, 32.67 ± 0.00 mJ/m^2, 33.56 ± 0.03 mJ/m^2, 33.60 ± 0.03 mJ/m^2 and 33.35 ± 0.04 mJ/m^2, respectively. Detailed values of $\gamma_s{}^d$, $\gamma_s{}^p$ and γ_s for Au leaf, PEDOT:PSS, PVdC and PET substrate can be found in Table 4.0. The interfacial energy values between Au leaf with PEDOT:PSS, PVdC and PET substrates ($W_{Au/sub}$) which were obtained from eq.6 are summarized in Table 4.0.

Finally, by using eq. 7, we found that the W of Au/PEDOT:PSS (66.22 ± 0.02 mJ/m^2) was slightly higher than the W of Au/PET (66.00 ± 0.03 mJ/m^2) and similar to the W of Au/PVdC (66.24 ± 0.02 mJ/m^2). Thus, the difference of W between Au/PEDOT:PSS and Au/PET; and between Au/PEDOT:PSS and Au/PVdC are 0.22 mJ/m^2 and 0.02 mJ/m^2, respectively. From the experimental results, we found that the Au leaf on the PET substrate was successfully transferred to the PEDOT:PSS surface (Fig. 4.2. a (i-ii)). However, when we tried to transfer the Au leaf from PVdC to the PEDOT:PSS surface, the Au leaf breaks from the PVdC surface and partially transferred to the PEDOT:PSS surface (Fig. 4.2. b (i-ii)). These results show that the differences of *W* more than 0.22 mJ/m^2 was sufficient to transfer the Au leaf from one substrate to another. On the other hand, the unsuccessful transfer of the Au leaf on PVdC substrate to the PEDOT:PSS surface can be explained by the insufficient difference of *W* between Au/PVdC and Au/PEDOT:PSS.

Table 4.0: Dispersive and polar components of surface free energy for each substrate, interfacial energy and work of adhesion between Au/PET and Au/PEDOT:PSS.

Substrate	γ_s^p **(mJ/m^2)**	γ_s^d **(mJ/m^2)**	γ_s **(mJ/m^2)**	$\gamma_{Au/sub}$ **(mJ/m^2)**	$W_{Au/sub}$ **(mJ/m^2)**
Au leaf	4.00 ± 0.00	28.67 ± 0.00	32.67 ± 0.00	-	-
PET	4.40 ± 0.02	28.95 ± 0.02	33.35 ± 0.04	0.01 ± 0.00	66.00 ± 0.03
PEDOT:PSS	4.50 ± 0.03	29.07 ± 0.05	33.56 ± 0.03	0.02 ± 0.00	66.22 ± 0.02
PVdC	4.66 ± 0.11	28.94 ± 0.09	33.60 ± 0.03	0.03 ± 0.01	66.24 ± 0.02

To further confirm that the theoretical calculations match the experimental results, we attempted to transfer the Au leaf from the PET substrate to the PVdC substrate (difference of *W* of 0.24 mJ/m^2), and found that the Au leaf is successfully transferred from the PET substrate to the PVdC substrate (Fig. 4.2. c (i-ii)). Based on these results, we conclude that the *W* is a useful parameter to choose the suitable supporting materials for successful transfer during lamination.

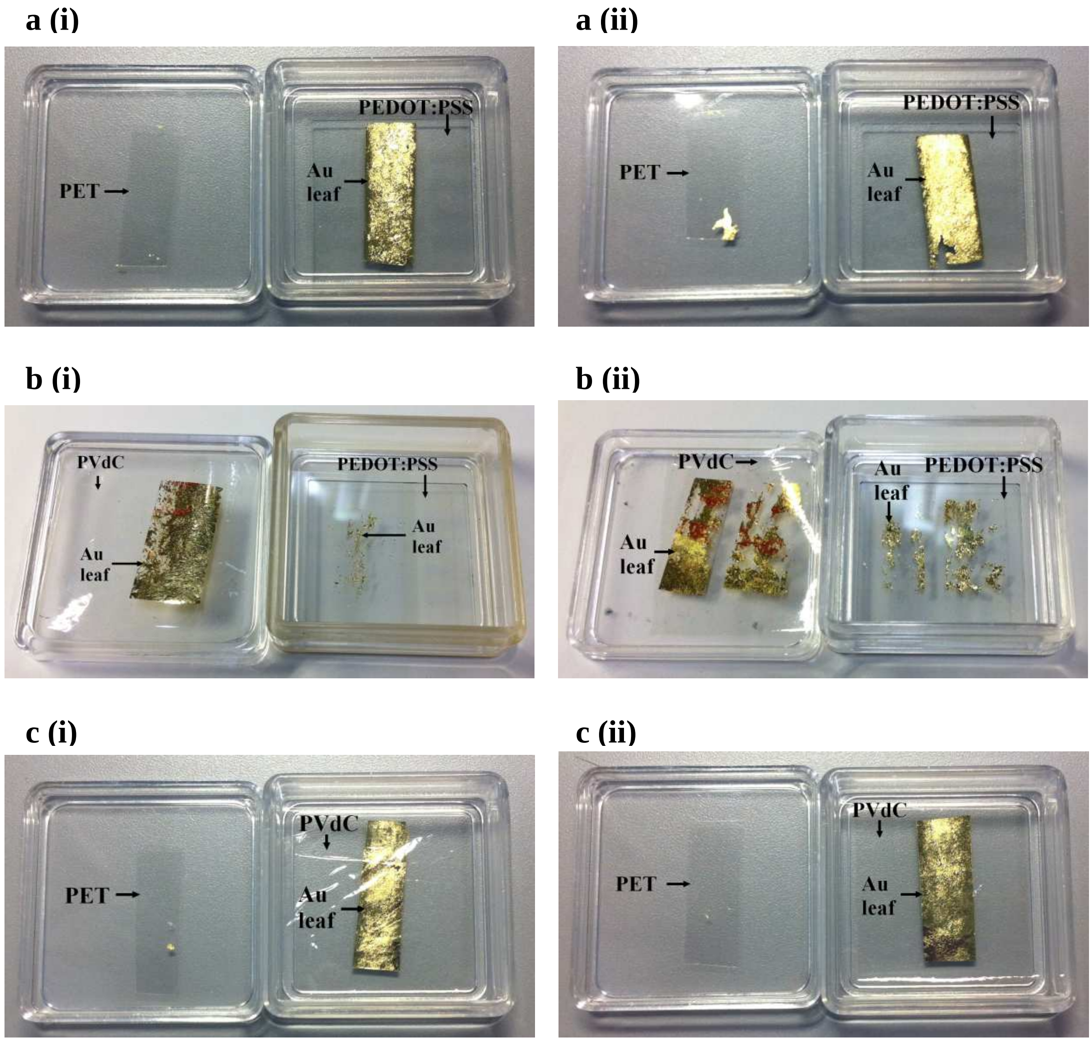

Fig. 4.2: The images of the successful transfer of Au leaf from PET to PEDOT:PSS (a (i-ii)), the unsuccessful transfer of Au leaf from PVdC to PEDOT:PSS (b (i-ii)) and the successful transfer of Au leaf from PET to PVdC (c (i-ii)).

4.3.2 Comparison in device performances between laminated and evaporated Au devices.

The current density - voltage (*J*-*V*) curves of evaporated Au metal and laminated Au leaf devices of P3HT:$PC_{61}BM$ system are shown in Fig. 4.3 and their PV parameters are summarized in Table 4.1. The evaporated Au devices exhibited 9.40 ± 0.80 mA/cm^2 of J_{sc}, 0.597 ± 0.005 V of V_{oc}, 0.568 ± 0.043 of FF, 5.29 ± 1.49

Ω.cm^2 of R_s and 3.19 ± 0.34% of PCE. For the Au leaf devices which are laminated at 100 ˚C, the J_{sc}, V_{oc}, FF, R_s and PCE are 7.74 ± 0.19 mA/cm^2, 0.592 ± 0.002 V, 0.565 ± 0.012, 6.55 ± 1.32 Ω.cm^2 and 2.59 ± 0.02% respectively. The J_{sc}, FF and R_s are related to the contact quality at the top electrode and to charge collection efficiency.[22,23] These device parameters in laminated devices suggest that their lower performances may be related to the contact condition at the Au/PEDOT:PSS interface.

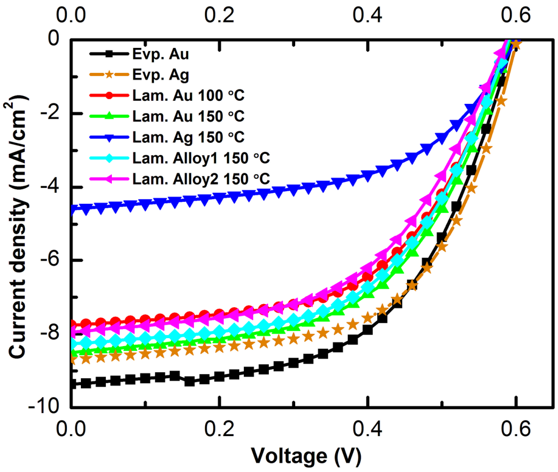

Fig. 4.3: *J*-*V* curves of evaporated and laminated P3HT:PC$_{61}$BM devices.

The images of the top electrode surfaces were taken using an optical microscope (Fig. 4.4). Evaporated Au electrode exhibited complete coverage of the Au on the surface of PEDOT:PSS (Fig. 4.4(a)) while laminated Au electrode showed some wrinkles as a result of inhomogeneous coverage between Au leaf/PEDOT:PSS interface (Fig. 4.4(c)). These wrinkles were already formed when the Au leaf was deposited on the supporting PET substrate (Fig. 4.4(b)) prior to the lamination process. By increasing the lamination temperature from 100 ˚C to 150 ˚C, the electrode showed better coverage of Au leaf on the PEDOT:PSS (Fig. 4.4(d)). At higher temperature, the modulus of elasticity of metal will decrease and the softer Au leaf thus spreads more smoothly on the PEDOT:PSS surface during lamination.[24] As a result, the parameters of the devices laminated at 150 ˚C increased to 8.28 ± 0.95 mA/cm^2 of J_{sc}, 0.593 ± 0.003 V of V_{oc}, 0.572 ± 0.025 of FF, 5.33 ± 0.87 Ω.cm^2 of R_s and 2.80 ± 0.28% of PCE.

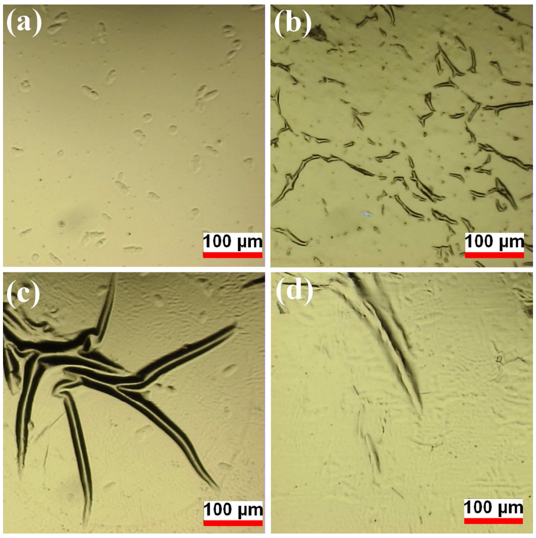

Fig. 4.4: Optical microscope images of the electrode surface. (a) Evaporated Au, (b) Au leaf on the PET substrate, (c) laminated Au leaf at 100 ˚C and (d) laminated Au leaf at 150 ˚C. The images were obtained with a 250 times magnification.

Table 4.1: Summary of solar cell characteristics of laminated and evaporated top electrode devices for P3HT:PC$_{61}$BM system.

Device	**Temperature (˚C)**	**J_{sc} (mA/cm^2)**	**V_{oc} (V)**	**FF**	**PCE (%)**	**R_s (Ω.cm^2)**
Evp. Au	-	9.40 ± 0.80	0.597 ± 0.005	0.568 ± 0.043	3.19 ± 0.34	5.29 ± 1.49
Lam. Au	100	7.74 ± 0.19	0.592 ± 0.002	0.565 ± 0.012	2.59 ± 0.02	6.55 ± 1.32
Lam. Au	150	8.28 ± 0.95	0.593 ± 0.003	0.572 ± 0.025	2.80 ± 0.28	5.33 ± 0.87
Evp. Ag	-	8.80 ± 0.29	0.602 ± 0.002	0.587 ± 0.013	3.11 ± 0.17	2.35 ± 0.28
Lam. Ag	150	4.07 ± 0.69	0.601 ± 0.003	0.537 ± 0.012	1.31 ± 0.25	7.71 ± 1.16
Lam. Alloy1	150	8.23 ± 0.29	0.590 ± 0.000	0.554 ± 0.017	2.69 ± 0.17	6.01 ± 0.37
Lam. Alloy2	150	7.90 ± 0.18	0.587 ± 0.001	0.536 ± 0.010	2.49 ± 0.07	10.19 ± 1.83

4.3.3 Effect of oxidation level to the device performances

To further reduce the cost of materials, Alloy1, Alloy2 and Ag leaves are applied as the electrode in the lamination process. These electrodes were laminated at 150 ˚C and characterized. The laminated Alloy1, Alloy2 and Ag exhibit low device performances (in descending order) as compared to that the laminated Au (Table 4.1). Unlike the evaporated devices, the laminated Ag devices show much lower performance than the laminated Au devices. Other than Au, other metals are easily oxidized when exposed to the oxygen, while evaporated electrode devices were deposited at very low pressure, around ×10^{-7} torr. In order to confirm the oxidation of alloys and Ag leaves, we measured the O1s intensity of these leaves by using X-ray photoelectron spectroscopy (XPS).

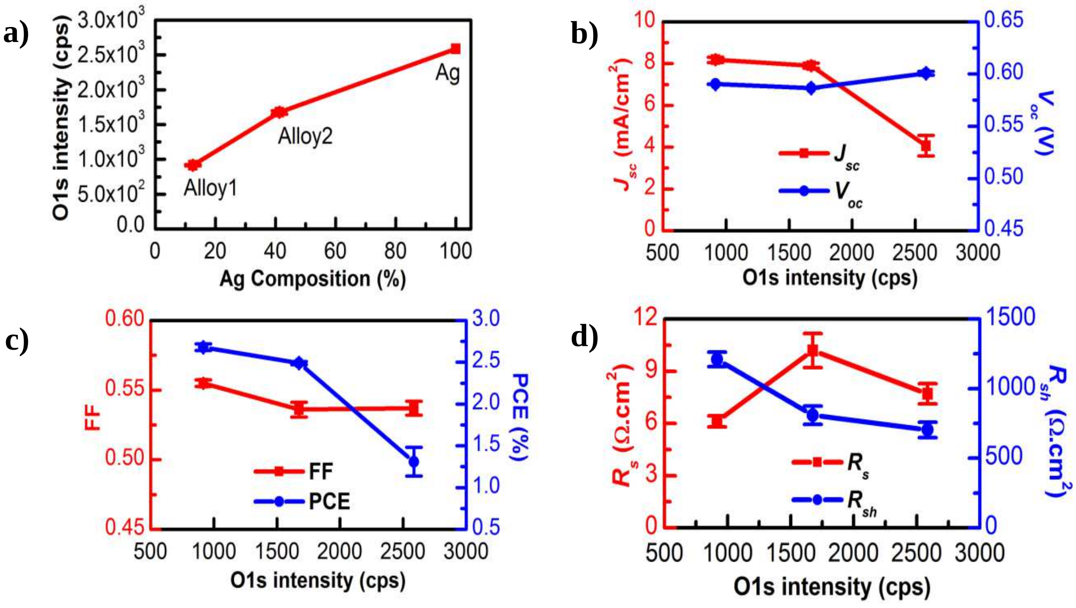

Fig. 4.5: Correlation between: (a) Ag compositon and oxidation level of Alloy1, Alloy2 and Ag leaves, (b) oxidation level and J_{sc}, V_{oc}, (c) oxidation level and FF, PCE and (d) oxidation level and R_s, R_{sh}.

Figure 4.5 shows the oxygen level for leaves that contains Ag metal and the relationship between oxygen level and device parameters. As the Ag composition increased, the oxidation level also increased (Fig. 4.5(a)). In general, when the oxidation level increased, the J_{sc}, FF, PCE, $R_{sh,}$and R_s degraded, while V_{oc} did not change much (Fig. 4.5(b-d)). This correlation shows that, oxidation is the reason for the inefficient device performances of laminated Alloy1, Alloy2 and Ag, as it affect the conductivity of the top electrode. Therefore, Alloy1, Alloy2 and Ag leaves are not suitable to become the electrode although their cost are lower than Au leaf.

4.3.4 Stability of the laminated devices

We further investigate their stability properties and find that both unencapsulated laminated and evaporated Au devices also demonstrate similar behavior under constant light irradiation up to 15 h. In inverted BHJ devices with TiO_x as an electron transporting layer, we can usually observe a light soaking effect (LSE). [25)] This LSE is resulted from the filling of the TiO_x electron traps when the devices are exposed to light irradiation thus enhancing the charge collection properties of TiO_x layer.[26,27)] Figure 4.6(a-b) shows that such LSE leads to the enhancement of solar cell properties of both laminated and evaporated Au electrode devices up to 5 min. However, after the initial increase, the PCE of the devices remain stable up to 3 h.

Throughout the measurement period, the degradation is only 10% and 13% for evaporated and laminated devices respectively. This similar stability trend indicates that the adhesion between Au leaf/PEDOT:PSS is strong and shows no sign of delamination, which confirms that contact quality of the laminated Au electrode is comparable to that of the evaporated Au electrode. At the same time, PEDOT:PSS layer acts as a barrier to prevent the oxygen from entering the active layer prior to top electrode deposition.[28)]

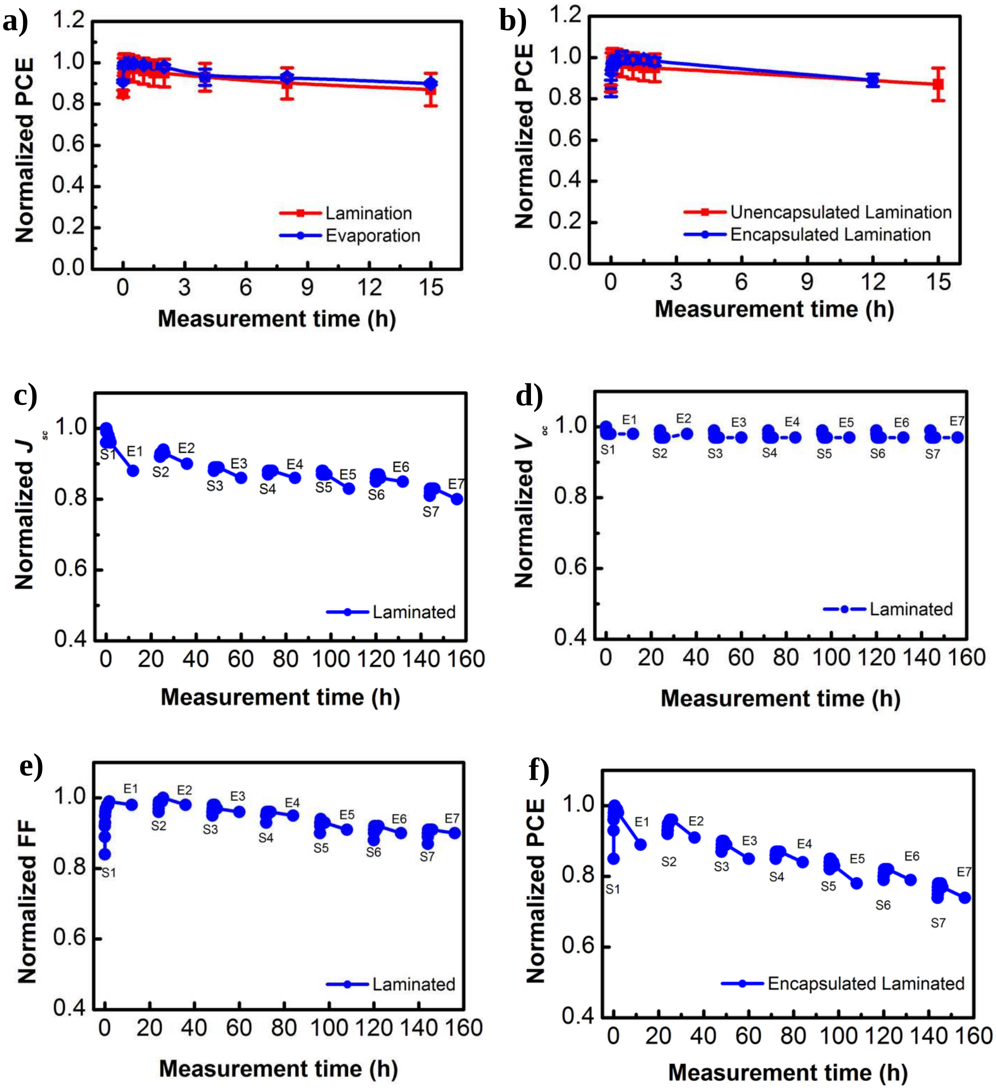

Fig. 4.6: Stability trend of normalized (a) PCE for unencapsulated evaporated and laminated devices, and (b) PCE for unencapsulated and encapsulated laminated devices under 15 h of continuous irradiation. (c) until (f) are the stability trend of normalized J_{sc}, V_{oc}, FF and PCE of the encapsulated laminated Au device under normal operation for 7 days. S1 and E1 represent start and end of measurement of day 1.

The efficiency of encapsulated and unencapsulated laminated devices are comparable as shown in Fig. 4.6(b). Based on this result, we measured the encapsulated laminated device by trying to simulate the daily operation of solar cells, which is 12 h under continuous irradiation and another 12 h under dark and this process repeated for 7 days. After 7 days of measurement, V_{oc} remained constant throughout the measurement. J_{sc} and FF of the device maintained about 80% and 90% of their stability, respectively, resulting in maintaining 70% of the device PCE stability (Fig 4.6(c-f)). J_{sc} value affected the most to the device PCE as compared to the FF and V_{oc}.

4.3.5 High performance of PNTz4T:$PC_{71}BM$ system device

With the emergence of high performance p-type polymers, the PCE of OSCs is constantly increasing. To demonstrate that the Au leaf lamination process is a promising technique to fabricate low-cost, high efficiency and stable devices, we have applied the Au laminated electrodes to other devices with p-type polymer: $PC_{71}BM$ active layer. We fabricated evaporated and laminated devices using PNTz4T.$^{29)}$

Table 4.2: Summary of PV characteristics for evaporated and laminated PNTz4T:$PC_{71}BM$ devices

Device	**J_{sc} (mA/cm^2)**	**V_{oc} (V)**	**FF**	**PCE (%)**	**R_s (Ω.cm^2)**
Evaporated	16.92 ± 0.99	0.699 ± 0.003	0.503 ± 0.001	5.95 ± 0.32	13.59 ± 0.71
Laminated	15.14 ± 0.25	0.726 ± 0.000	0.461 ± 0.012	5.07 ± 0.22	14.17 ± 1.19

Figure 4.7(a) and (b) show the chemical structure of PNTz4T polymer and *J*-*V* curves of both evaporated and laminated devices respectively. The solar cell parameters of both evaporated and laminated devices are comparable. PNTz4T

polymer has a broad absorption range up to 800 nm which contribute to higher J_{sc} value (Fig. 4.7 (c)) compared to that of the P3HT polymer. Table 4.2 summarizes the device performances which exhibiting PCE of 5.95 ± 0.32% and 5.07 ± 0.22% of evaporated and laminated devices respectively. With PNTz4T, our laminated devices reach PCE up to 5.07 ± 0.22%, which correspond to the highest PCE reported for the laminated devices.8)

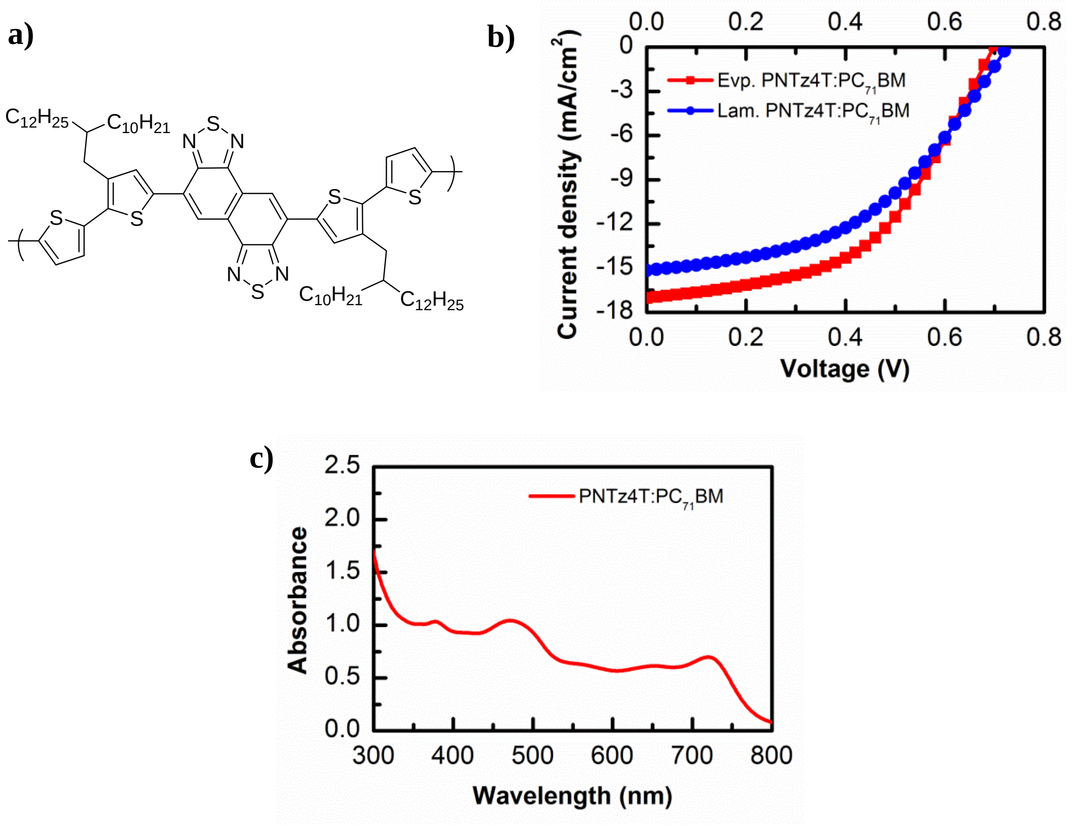

Fig. 4.7: (a) Chemical structure of PNTz4T polymer, (b) *J*-*V* curves of evaporated and laminated Au electrodes, and (c) absorption spectra of PNTz4T:PC$_{71}$BM film.

4.3.6 Comparison in fabrication cost between evaporated and laminated Au electrodes

One of the reasons roll-to-roll process become favourable over vacuum evaporation process is the low production cost (time and materials). A study in estimating the manufacturing cost of OSC was reported.30) In this part, the cost comparison between using evaporated Au and laminated Au leaf electrode based on our vacuum deposition machine and electrode size are made and shown in Table 4.3.

Table 4.3: Summary of electrode fabrication cost between evaporation and lamination process.

Materials	Price	No. of substrates / process	Price / substrates
Au wire	¥ 4872.71 / g	9 / evaporation	¥ 378.99
Au leaf	¥ 288.7 / sheet	175 / sheet	¥ 1.65

1 g of pure Au cost about ¥ 4872.71 and for one evaporation process it requires about 0.7 g of Au (¥3410.9) to get thickness of 100 nm. Our vacuum evaporation machine can accommodate 9 substrates at one batch.This means that, the cost is about ¥ 378.99 per substrate. On the other hand, the price of one sheet of Au leaf with an area of 210.25 cm^2 is only ¥ 288.70. By considering 2 electrodes per substrate is 1.2 cm^2 (0.6 cm^2 per electrode), we can get 175 substrates per sheet. It cost about ¥ 1.65 per substrate, which is about 200 times cheaper than the evaporated Au. This implies that, the lamination using metal leaf is very cost effective than the vacuum evaporation process.

Using Au leaf, combined with the lamination process presents a major advantage over the evaporation process as it reduces the production cost by removing the losses of materials on the evaporation chamber walls.20) The time required to form the electrodes can be shortened drastically as it takes only 5 min to deposit metal leaves electrodes.

4.4 Spray coating of Au ink NPs

4.4.1 Fabrication and characterization of regular BHJ device

Glass ITO substrates were cleaned using the standard cleaning process described here: sonication in acetone (5 min), semico clean (10 min), pure water (10 min), IPA (10 min), followed by IPA vapour exposure (3 min) and UV ozone treatment (30 min). 30 mg/ml of P3HT:PCBM solution with 1:1 ratio in chlorobenzene was prepared and stirred for 4 h in nitrogen filled glove box. With 0.1 µm filter, PEDOT:PSS solution was spin coated on top of the ITO substrate at 1600 rpm for 60 s with a 2 s slope and dried at 200 ˚C for 10 min, resulting in a 75 nm thick layer. The P3HT:PCBM solution was then spin coated at 800 rpm for 60 s with 0.20 µm filter inside the glove box which formed 120 nm thick film (Fig. 4.8 (a)). The substrates then pre-annealed at 120 ˚C for 10 min prior to the electrodes deposition. The electrodes were deposited by spray coating Au ink NPs (Fig. 4.8 (b)). For reference devices, the aluminum electrodes were vacuum deposited. After depositing the electrodes, the solar cell parameters were measured before and after annealing at 140 ˚C for 10 min using a sourcemeter (Keithley 2400) and a solar simulator (AM 1.5G, 100 mW/cm^2) at room temperature.

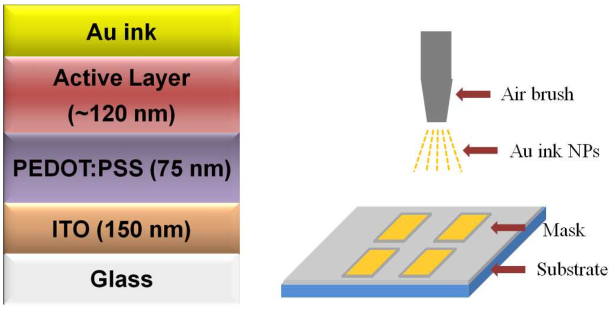

a) **b)**

Fig. 4.8: Schematic representation of (a) regular device architecture and (b) spray coating process.

4.4.2 Performance of spray coating Au NPs ink

The *J*-*V* curves for spray coating Au NPs ink and evaporated Al electrodes before and after annealing for regular BHJ devices are shown in Fig. 4.9 and the solar cell parameters are summarized in Table 4.4.

The PCE of spray coating devices decreased after annealing, from 0.23% to 0.17%, mainly due to the decreased in J_{sc} and V_{oc}, from 3.20 mA/cm^2 to 2.65 mA/cm^2 and from 0.268 V and 0.237 V, respectively. The FF did not change much after annealing. These results are in contrast as compared to that of the reference evaporated device, where the PCEs have improved from 1.40% to 2.47% after annealing.

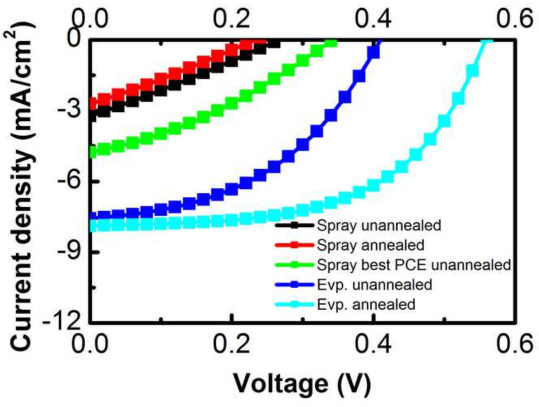

Fig. 4.9: *J*-*V* curves for spray coated Au ink NPs and evaporated Al electrode devices.

Table 4.4: Summary of solar cell parameters for spray coating Au ink NPs and evaporated Al electrode devices.

Deposition method	Annealing condition	J_{sc} (mA/cm2)	V_{oc} (V)	FF	PCE (%)
Spray Au NPs	**Unannaled**	3.20	0.268	0.269	0.23
	Annealed	2.65	0.237	0.274	0.17
	Unannealed (best)	4.78	0.346	0.326	0.54
Evaporated Al	**Unannealed**	7.57	0.419	0.441	1.40
	Annealed	7.89	0.565	0.554	2.47

One of the possible reasons that could contribute to this degradation and low performance is the Au ink work function increased to 4.43 eV after annealing at 140 ˚C for 10 min. The surface of the spray coating electrode also was not smooth and did not cover entirely the active layer surface (Fig. 4.7). The highest PCE obtained by using spray coating Au ink is 0.54%.

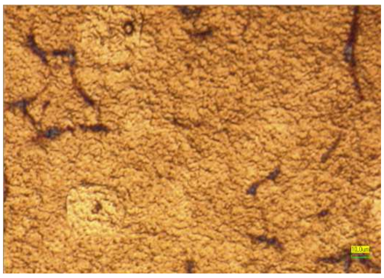

Fig. 4.7: Surface of the spray coating Au ink NPs

4.5 Chapter conclusions

In conclusion, we successfully fabricated efficient and stable inverted BHJ solar cells using Au leaf as a laminated top electrode, which completely removes the use of the costly vacuum evaporation process. We have proven that the Au leaf was successfully transferred from the supporting PET substrate to the PEDOT:PSS surface due to the difference in *W* values between Au/PEDOT:PSS and Au/PET. By employing the *W*, we can choose a suitable material as a supporting substrate for the successful lamination. The homogeneous coverage between laminated Au electrode and PEDOT:PSS can be improved by increasing the lamination temperature. The stability of the unencapsulated laminated Au device is comparable to that of the evaporated Au ones. Using PNTz4T:$PC_{71}BM$ system, Au laminated device achieves high PCE up to 5.07%. Therefore, lamination using Au leaf has the potential to overcome vacuum evaporation as a low cost alternative manufacturing process to produce efficient and stable devices. On the other hand, devices that fabricated by spray coating of Au NPs electrodes are worked, although the performances are lower compared to that the reference evaporated Al electrode device.

4.6 References

[1]F. C. Krebs, Org. Electron. **10**, 761 (2009).

[2] W. Gaynor, J. Y. Lee and P. Peumans, ACS Nano **4**, 30 (2010).

[3]G. Chidichimo and L. Filippelli, Int. J. Photoenergy **2010**, 5201 (2010).

[4]J. Nelson, Mater. Today. **14**, 462 (2011).

[5]F. C. Krebs, J. Alstrup, H. Spanggaard, K. Larsen and E. Kold, Sol. Energy Mater. Sol. Cells. **83**, 293 (2004).

[6]F. C. Krebs, Sol. Energy Mater. Sol. Cells. **93**, 465 (2009).

[7]M. Granström, K. Petritsch, A. C. Arias, A. Lux, M. R. Andersson and R. H. Friend, Nature. **395**, 257 (1998).

[8]Y. Yuan, Y. Bi and J. Huang, Appl. Phys. Lett. **98**, 063306 (2011).

[9]R. Søndergaard, M. Hösel, D. Angmo, T. T. Larsen-Olsen and F. C. Krebs, Mater. Today. **15**, 36 (2012).

[10]J. Huang, G. Li and Y. Yang, Adv. Mater. **20**, 415 (2008).

[11]M. Nakamura, C. Yang, K. Tajima and K. Hashimoto, Sol. Energy Mater. Sol. Cells. **93**, 1681 (2009).

[12]B. A. Bailey, M. O. Reese, D. C. Olson, S. E. Shaheen and N. Kopidakis, Org. Electron. **12**, 108 (2011).

[13]J. Zaumseil, K. W. Baldwin and J. A. Rogers, J. Appl. Phys. **93**, 6117 (2003).

[14]Y.-F. Lim, S. Lee, D.J. Herman, M.T. Lloyd, J.E. Anthony, and G.G. Malliaras, Appl. Phys. Lett. **93**, 193301 (2008).

[15]S.K. Hau, H.-L. Yip, K. Leong, and A.K.-Y. Jen, Org. Electron. **10**, 719-723 (2009).

[16]J. K. Kim, W. Kim, D. H. Wang, H. Lee, S. M. Cho, D. G. Choi and J. H. Park, Langmuir. **29**, 5377 (2013).

[17]J. Kim, D.-Y. Khang, J.-H. Kim, and H.H. Lee, Appl. Phys. Lett. **92**, 133307 (2008).

[18]S. R. Dupont, M. Oliver, F. C. Krebs and R. H. Dauskardt, Sol. Energy Mater. Sol. Cells. **97**, 171 (2012).

[19]T. Kuwabara, H. Sugiyama, M. Kuzuba, T. Yamaguchi and K. Takahashi, Org. Electron. **11**, 1136 (2010).

[20]Y. Ding, Y. J. Kim and J. Erlebacher, Adv. Mater. **16**, 1897 (2004).

[21]D. K. Owens and R. C. Wendt, J. Appl. Polym. Sci. **13**, 1741 (1969).

[22]N. Grossiord, J. M. Kroon, R. Andriessen and P. W. M. Blom, Org. Electron. **13**, 432 (2012).

[23]J. D. Servaites, S. Yeganeh, T. J. Marks and M. A. Ratner, Adv. Funct. Mater. **20**, 97 (2010).

[24]A. A. Volinsky, N. R. Moody and W. W. Gerberich, J. Mater. Res. **19**, 9 (2004).

[25]Z. Wang, R. Xing, X. Yu and Y. Han, Nanoscale, **3**, 2663 (2011).

[26]C. S. Kim, S. S. Lee, E. D. Gomez, J. B. Kim and Y. L. Loo, Appl. Phys. Lett. **94**, 113302 (2009).

[27]T. Kuwabara, C. Iwata, T. Yamaguchi and K. Takahashi, ACS Appl. Mater. Inter. **2**, 2254 (2010)

[28]S. K. Hau, H. L. Yip, N. S. Baek, J. Zou, K. O’Malley and A. K. Y. Jen, Appl. Phys. Lett. **92**, 253301 (2008).

[29]I. Osaka, M. Shimawaki, H. Mori, I. Doi, E. Miyazaki, T. Koganezawa and K. Takimiya, J. Am. Chem. Soc. **134**, 3498 (2012).

[30]J. Kalowekamo and E. Baker, Sol. Energy, **83**, 1224 (2009).

CHAPTER 5: CONCLUSIONS AND FUTURE WORKS

5.1 Conclusions

Through this thesis, the development of efficient and low cost OSC device in terms of controlling the morphological changes, and device fabrication methods for efficient and low cost OSC are investigated. In this investigation, the aims were, firstly to study the factors that contribute to the device efficiency, through thermal annealing, which could lead to polymer crystallization and phase segregation and by insertion of interlayer which affect the active layer morphology. Secondly, to fabricate the OSC device by implementing vacuum free top electrode deposition process.

Our results have shown that devices that were post-annealing after top electrode deposition have increased the solar cell performances significantly as compared to that of the devices without post-annealing. Post-annealing induced polymer crystallization and resulting in enhancement in the absorption. Vertical phase segregation also could occur as a result of annealing as shown in EDS images. In regular BHJ, both polymer crystallization and vertical phase segregation contributed to the better device performance, whereas in the inverted BHJ, the concentration gradient remains unchanged after annealing because of the insertion of the HTL and ETL which give high V_{oc} even before annealing. Therefore, the increased in inverted device performances is due to the polymer crystallization. The OSC device performance can be further enhanced by inserting interlayer such as PEDOT:PSS which acts as both HTL and electron blocking layer, and TiO_x which function as ETL as well as hole blocking layer. These interlayers promoted charge collection, prevent charge recombination and current leakage.

It was also shown that the standard vacuum evaporation process has been successfully replaced with the Au leaf lamination process. By quantifying the *W* between Au/supporting substrate and Au/PEDOT:PSS, ones can choose the appropriate supporting substrate for Au leaf prior to the device fabrication to ensure the Au leaf transfer completely to the PEDOT:PSS film surface. Better Au leaf coverage can be obtained by increasing the lamination temperature, thus increased the device performance. Laminated Au devices exhibit similar stability with the evaporated Au devices. By using PNTz4T:$PC_{71}BM$ system, the laminated Au devices achieved 5.07% of PCE, which is among the highest PCE for vacuum free devices so far. This lamination process reduced the fabrication time and waste materials, which are the advantages over vacuum evaporation process.

In conclusion, we have shown that efficient and low cost OSC can be achieved through the fabrication processes development; both morphological control and vacuum free deposition process.

5.2 Future works

Nowadays, flexible OSC is on demand and research about it is still ongoing. The research that are done not only to obtain a low cost device but also higher efficiency. The lamination condition such as pressure and temperature can be further optimized in flexible substrate in order to achieve more homogeneous lamination surface. We could further minimize the material cost by stacking a thin layer of Au leaf to another layer metal leaf. The surface treatment can be done to the metal and alloy leaves to remove the contamination and oxidation that exist on their surfaces. This lamination process, not only suitable for top electrode deposition process, but also can be implemented in other functional layers to fabricate fully vacuum free OSC devices. Other processes that are compatible for roll-to-roll process can be further improved to obtain both efficient and low cost devices. As for the Au leaf, it can be used as metal electrodes in other organic electronic devices such as organic light emitting diode (OLED).